Faculty of Physics and Astronomy
Heidelberg University

Bachelor Thesis

in Physics

submitted by

Valentin Hell

born in Heilbronn

2024

The influence of a periodic electric bias field on the dielectric loss of atomic tunneling systems in the borosilicate glass BS 3.3

This bachelor thesis was conducted by Valentin Hell
at the Kirchhoff-Institute for Physics
under the supervision of
Prof. Dr. C. Enss

In this thesis the influence of a periodic electric bias field on the dielectric loss of atomic tunneling systems in the borosilicate glass BS 3.3 is investigated at a temperature of 30 mK. For that a superconducting LC-resonator was microstructured onto the glass sample to probe the tunneling systems in the sample at a resonance frequency of 1.125 GHz. Additionally, a cover electrode on the sample allows for the application of an electric bias field which induces non-equilibrium Landau-Zener dynamics of the tunneling systems and thus changes the dielectric loss. The dielectric response of the tunneling systems was measured at bias rates between $10^{-3}\,\frac{\mathrm{MV}}{\mathrm{m{\cdot}s}}$ and $10^{4}\,\frac{\mathrm{MV}}{\mathrm{m{\cdot}s}}$ and at bias voltages ranging from 0.1 V to 20 V. At low bias rates the dielectric loss reaches the saturation limit and increases at higher bias rates for all bias voltages. As expected, the return to the saturation limit at the highest bias rates can only be observed at low bias voltages. At higher bias voltages the dielectric loss does not drop back to the saturation limit within the measured bias rate range but reaches the fully desaturated limit of the single ramp regime. The decrease of the dielectric loss at high bias rates and bias voltages can be addressed to a heating of the sample. Additionally, an average dipole moment of $p = 0.31\,\mathrm{D}$ and an average lifetime of the tunneling systems' excited state of $\tau \approx 13\,\mu\mathrm{s}$ were obtained from the measurement results.

Der Einfluss eines periodischen elektrischen Vorspannungsfeldes auf den dielektrischen Verlust atomarer Tunnelsysteme im Borosilikatglas BS 3.3

In dieser Arbeit wird der Einfluss eines periodischen elektrischen Vorspannunsfeldes auf den dielektrischen Verlust atomarer Tunnelsysteme im Borosilikatglas BS 3.3 bei einer Temperatur von 30 mK ermittelt. Dafür wurde ein supraleitender LC-Reonator auf die Glasprobe mikrostrukturiert, um die Tunnelsysteme in der Probe bei einer Resonanzfrequenz von 1,125 GHz zu untersuchen. Zusätzlich ermöglicht eine Deckelektrode auf der Probe das Anlegen eines elektrischen Vorspannungsfeldes, welches Nicht-Gleichgewichts-Landau-Zener-Dynamiken der Tunnelsysteme induziert und somit den dielektrischen Verlust verändert. Die dielektrische Antwort der Tunnelsysteme wurde bei Vorspannungsraten zwischen $10^{-3}\,\frac{\mathrm{MV}}{\mathrm{m{\cdot}s}}$ und $10^{4}\,\frac{\mathrm{MV}}{\mathrm{m{\cdot}s}}$ und bei Vorspannungen von $0,1\,\mathrm{V}$ bis 20 V gemessen. Bei niedrigen Vorspannungsraten erreicht der dielektrische Verlust das Sättigungslimit und steigt bei höheren Vorspannungsraten bei allen Vorspannungen an. Wie zu erwarten kann der Rückgang zum Sättigungslimit bei hohen Vorspannungsraten nur bei niedrigen Vorspannungen beobachtet werden. Bei hohen Vorspannungen fällt der dielektrische Verlust im gemessenen Vorspannungsratenbereich nicht auf das Sättigungslimit ab, sondern erreicht das vollständig entsättigte Limit des Einzelrampenbereichs. Die Abnahme des dielektrischen Verlusts bei hohen Vorspannungsraten und -spannungen kann auf eine Erwärmung der Probe zurückgeführt werden. Zusätzlich ließ sich aus den Messergebnissen ein mittleres Dipolmoment von $p = 0,31\,\mathrm{D}$ und eine mittlere Lebensdauer des angeregten Zustands der Tunnelsysteme von $\tau \approx 13\,\mu\mathrm{s}$ ermitteln.

Contents

1 Introduction **1**

2 Theoretical Background **3**

2.1 Low temperature properties of glasses 3

2.2 Standard Tunneling Model 4

2.3 Dielectric properties of glasses at low temperatures 6

2.3.1 Dielectric function 6

2.3.2 Interaction of a two-level system with an electric field 8

2.3.3 Relaxation processes 9

2.3.4 Resonant processes 10

2.3.5 Parameter distribution 11

2.3.6 Saturation by large electric fields 15

2.4 Non-equilibrium loss and Landau-Zener transitions 15

2.4.1 Single ramp biasing 18

2.4.2 Continuous biasing 20

3 Experimental Methods **25**

3.1 Measurements at low temperatures 25

3.2 Setup for measuring the dielectric response 26

3.3 Resonator and sample 26

3.4 Measurement principle 28

3.4.1 Application of a continuous electric bias signal 30

4 Experimental Results **33**

4.1 Power dependency 33

4.2 The dielectric loss in terms of the bias rate 34

4.2.1 Two dimensional map of the dielectric loss 37

4.3 The dielectric loss in terms of the dimensionless bias rate 39

5 Summary and Outlook **43**

Bibliography **45**

1. Introduction

In contrast to crystals in which a periodic order of atoms and therefore a long range order exists, the atoms in amorphous solids are disordered resulting in the existence of only a short range order [Hun74]. At low temperatures, the thermal properties of solids are determined by long-wavelength phonons. Since long-wavelength phonons are unaffected by the microscopic structure they do not only exist in crystals but also in amorphous solids. Therefore, the Debye model [Deb12] should in principle describe the thermal properties of both crystals and amorphous solids at low temperatures. However, in 1971 Zeller and Pohl [Zel71] found out that glasses, which are a subgroup of amorphous solids, behave very differently from their crystalline counterparts at low temperatures. More precisely, they found a different temperature dependency of the specific heat capacity and the thermal conductivity that both deviate significantly from their crystalline versions. This resulted in a major effort being made to gain a better understanding of amorphous solids at low temperatures. Only one year later Anderson *et al.* [And72] and Phillips [Phi72] developed the standard tunneling model (STM) in which they suggested a broad distribution of atomic two-level systems to be responsible for this deviating behavior. In this model atoms or groups of atoms can only change their state by quantum mechanical tunneling between the two states at low temperatures. These low-energy excitations explained the deviating thermal properties of glasses observed by Zeller and Pohl [Zel71] quite well. Furthermore the STM is successful in predicting experimental findings in dielectric [vS77, Fro77, Rog97], acoustic [Cla94, Cla00] and ultrasonic absorption [Hun72, Hun77] measurements of amorphous solids. However, the STM only gives a phenomenological explanation for the thermal properties of amorphous solids at low temperatures and the question of the microscopic origin of the low-energy excitations still remains unanswered.

Recently, the research on tunneling systems gained increasing interest because they act as a major source of noise [Bur14, Nei13] and decoherence [Ku05, Mü19] in superconducting quantum devices. Therefore, it is crucial to gain a deeper understanding of the behavior of tunneling systems at low temperatures. In this sense superconducting microwave resonators were used to measure the dielectric response of tunneling systems. Khalil [Kha13] and Frey [Fre21] used additional electric bias fields to induce Landau-Zener dynamics of tunneling systems.

In this thesis a periodic electric bias field is used to induce Landau-Zener dynamics of the tunneling systems in the borosilicate glass BS 3.3. This is realized by placing a superconducting LC-resonator and a cover electrode that applies the bias field directly onto the bulk glass.

The thesis at hand is structured as follows:
Chapter 2 contains the theoretical background which is essential for the understanding of the performed measurements. After briefly presenting the behavior of amorphous solids at low temperatures the standard tunneling model is introduced to explain these properties. Then we focus on the dielectric properties of glasses in the context of the behavior of tunneling systems under the influence of high-frequency electric fields and electric bias fields which induce Landau-Zener dynamics. In chapter 3 the experimental methods used in this thesis are presented including the high-frequency setup and the resonator which are used to measure the dielectric response of the tunneling systems in the glass sample. In chapter 4 the results of the power dependency measurements and the non-equilibrium measurements are presented and interpreted within the standard tunneling model and the Landau-Zener theory. In the end, chapter 5 summarizes the results and gives an outlook on future experiments.

2. Theoretical Background

This chapter contains the theoretical background which is essential for the understanding of the performed measurements and the results concluded from them. First the standard tunneling model is introduced to explain the behaviour of glasses at low temperatures. We continue with dielectric properties of glasses and end this chapter with an introduction of the Landau-Zener formalism to describe the non-equilibrium dynamics of biased tunneling systems.

2.1 Low temperature properties of glasses

A crystal consists of periodically arranged unit cells which are made up by a well defined arrangement of atoms leading to the existence of a long range order. In an amorphous solid on the other hand, the atoms form a disordered structure where atomic distances and bond angles vary statistically so that only a short range order exists [Hun74]. However, the chemical composition of both versions can be the same. Glasses are a subgroup of amorphous solids but as this thesis only deals with glasses the terms amorphous solid and glass will be used equivalently.
Figure 2.1 shows the two-dimensional projection of the atomic structure of SiO_2 as a crystal (left) and as an amorphous solid (right). The disorder of amorphous solids results in a different behavior at low temperatures. For crystalline solids the specific heat capacity follows $C_\mathrm{V} \propto T^3$ at low temperatures according to Debye [Deb12]. The thermal conductivity is therefore also $\kappa \propto T^3$ because of $\kappa = \frac{1}{3} C_\mathrm{V} v_\mathrm{s} l$ if a constant sound velocity v_s and a free phonon gas with a constant mean free path l are assumed. However, an approximately linear temperature dependence of the specific heat capacity has been observed by Zeller and Pohl [Zel71] for glasses. They also found out that the specific heat capacity in glasses is much larger and independent of the chemical composition. Furthermore Zeller and Pohl determined a quadratic temperature dependence of the thermal conductivity which is a few magnitudes lower in glasses than in crystals. In the next chapter we will see that in glasses there are additional low energy excitations which are responsible for these deviations at low temperatures.

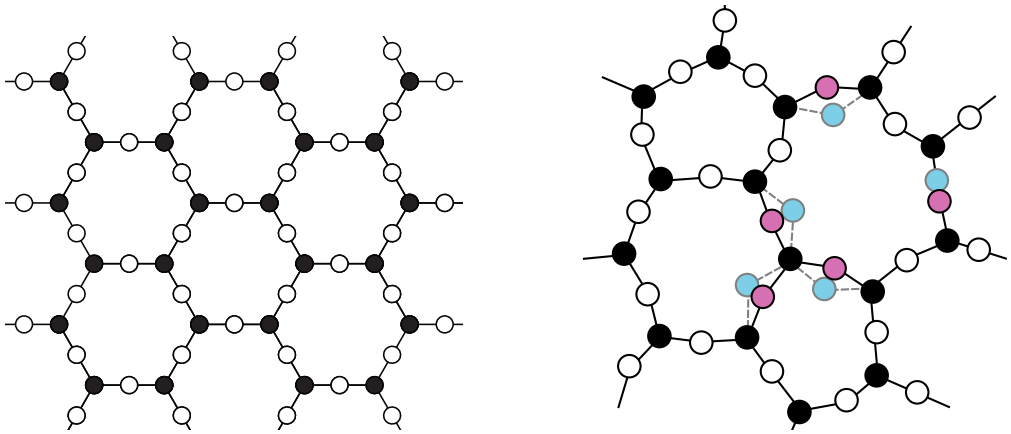

Figure 2.1: Two-dimensional projection of the crystal lattice of SiO_2 (left) and the structure of SiO_2 as an amorphous solid (right). The disordered structure results in different possible equilibrium positions of some atoms or groups of atoms. Adapted from [Zac32, Hun74].

2.2 Standard Tunneling Model

The differing properties of crystals and glasses at low temperatures can be explained by the standard tunneling model (STM) which was independently developed by Anderson *et al.* [And72] and Phillips [Phi72] in 1972. In this model they suggested the existence of atomic two-level systems in which atoms or groups of atoms can occupy different equilibrium positions.
A visual representation of two-level systems can be seen in figure 2.1 (right) where two possible equilibrium positions are marked with different colors for a few atoms. At low temperatures ($T \lesssim 1\,\mathrm{K}$) the potential barrier between such two levels can only be crossed by means of tunneling because it is too high to be crossed by thermal activation.
A two-level system can be represented by an asymmetric double-well potential in the energy space as can be seen in figure 2.2. V is the barrier height, Δ is the asymmetry energy which is the difference of the energy of the two equilibrium positions and d is the distance of the two equilibrium positions in the configuration space. The tunneling object has the mass m.
To find the eigenstates of the two-level system we have to solve the stationary Schrödinger equation

$$\hat{H}\psi = E\psi \quad . \tag{2.1}$$

Using the ansatz of a superposition of the wavefunctions of the uncoupled single well states ψ_a and ψ_b

$$\psi = a\psi_\mathrm{a} + b\psi_\mathrm{b} \tag{2.2}$$

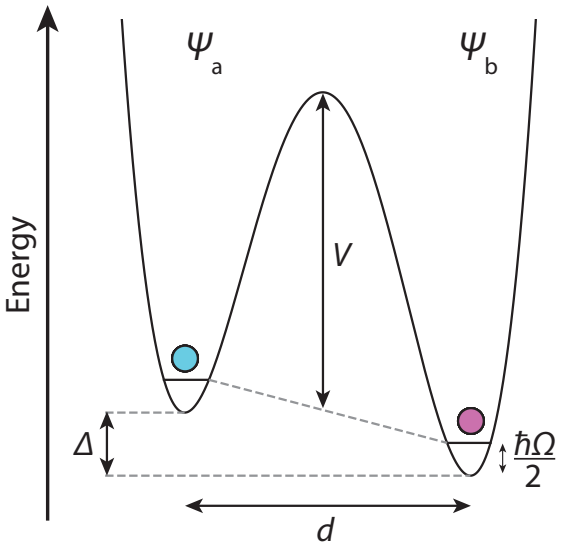

Figure 2.2: Double-well potential with a barrier height V, the asymmetry energy Δ and the well distance d. The individual single wells have the ground state energy $\frac{\hbar\Omega}{2}$. Adapted from [Phi81].

we obtain an upper limit of the energy eigenvalue of

$$E \leq \frac{\langle\psi|\,\hat{H}\,|\psi\rangle}{\langle\psi|\psi\rangle} = \frac{a^2 E_{\mathrm{aa}} + b^2 E_{\mathrm{bb}} + 2abE_{\mathrm{ab}}}{a^2 + b^2 + 2abS} \tag{2.3}$$

where we used $E_{\mathrm{aa}} = \langle\psi_{\mathrm{a}}|\,\hat{H}\,|\psi_{\mathrm{a}}\rangle$, $E_{\mathrm{bb}} = \langle\psi_{\mathrm{b}}|\,\hat{H}\,|\psi_{\mathrm{b}}\rangle$, $E_{\mathrm{ab}} = \langle\psi_{\mathrm{a}}|\,\hat{H}\,|\psi_{\mathrm{b}}\rangle$ and $S = \langle\psi_{\mathrm{a}}|\psi_{\mathrm{b}}\rangle$. By minimizing the total energy ($\frac{\partial E}{\partial a} = 0$ and $\frac{\partial E}{\partial b} = 0$) and choosing the zero point of the energy sitting between the two wells ($E_{\mathrm{aa}} = \frac{\hbar\Omega+\Delta}{2}$ and $E_{\mathrm{bb}} = \frac{\hbar\Omega-\Delta}{2}$) we obtain the two energy eigenvalues

$$E_{\mathrm{e,g}} = \frac{1}{2}\left(\hbar\Omega \pm \sqrt{\Delta^2 + 4E_{\mathrm{ab}}^2}\right) \tag{2.4}$$

if we assume that the two wells are so far apart that the overlap S is so small that it can be neglected. The energy splitting, denoted as E, is the difference of the energy of the two eigenstates:

$$E = E_{\mathrm{e}} - E_{\mathrm{g}} = \sqrt{\Delta^2 + 4E_{\mathrm{ab}}^2} = \sqrt{\Delta^2 + \Delta_0^2} \quad . \tag{2.5}$$

The tunneling splitting $\Delta_0 = -2E_{\mathrm{ab}}$ is the coupling energy between the two wells and can be expressed as

$$\Delta_0 = \hbar\Omega e^{-\lambda} \tag{2.6}$$

in the WKB[1] approximation where λ is the tunneling parameter that reads as

$$\lambda \approx \frac{d}{2\hbar}\sqrt{2mV} \quad . \tag{2.7}$$

[1] named after Wentzel, Kramers and Brillouin

By ignoring the constant offset $\frac{\hbar\Omega}{2}$ the Hamiltonian of the two-level system can be represented as

$$\hat{H} = \frac{1}{2}\begin{pmatrix} \Delta & -\Delta_0 \\ -\Delta_0 & -\Delta \end{pmatrix} \tag{2.8}$$

in the basis of the uncoupled states $|\psi_\mathrm{a}\rangle$ and $|\psi_\mathrm{b}\rangle$. Using the rotation matrix $\hat{R}_\phi$ and its inverse $\hat{R}_\phi^{-1}$

$$\hat{R}_\phi = \begin{pmatrix} \cos\phi & -\sin\phi \\ \sin\phi & \cos\phi \end{pmatrix} \quad \text{and} \quad \hat{R}_\phi^{-1} = \begin{pmatrix} \cos\phi & \sin\phi \\ -\sin\phi & \cos\phi \end{pmatrix} \tag{2.9}$$

the Hamiltonian can be diagonalized if we choose $\phi = \frac{1}{2}\arctan(\frac{\Delta_0}{\Delta})$:

$$\hat{\mathcal{H}} = \hat{R}_\phi \hat{H} \hat{R}_\phi^{-1} = \frac{1}{2}\begin{pmatrix} E & 0 \\ 0 & -E \end{pmatrix} \quad . \tag{2.10}$$

This results in the Hamiltonian $\hat{\mathcal{H}}$ being in the basis of the coupled states $|\Psi_\mathrm{g}\rangle$ and $|\Psi_\mathrm{e}\rangle$. The wavefunctions of the coupled states can be transformed back by writing them in terms of the wavefunctions of the uncoupled states:

$$\Psi_\mathrm{g} = \cos(\phi)\psi_\mathrm{a} + \sin(\phi)\psi_\mathrm{b} \tag{2.11}$$

$$\Psi_\mathrm{e} = -\sin(\phi)\psi_\mathrm{a} + \cos(\phi)\psi_\mathrm{b} \quad . \tag{2.12}$$

These two wavefunctions are shown in figure 2.3 where they are separated by the energy splitting E. When the tunneling object is in its ground state it is more likely to be found in the lower well. Conversely, if the tunneling object is in its excited state it has a higher probability to be in the upper well.

2.3 Dielectric properties of glasses at low temperatures

After we have only dealt with a static tunneling system so far we will now consider a tunneling system under the influence of an electric field. In this section the dielectric function and the contributions of relaxational and resonant processes are introduced. Then the discussion is extended to the influence of an electric field on an ensemble of tunneling systems as it exists in glasses. In the end, we consider how tunneling systems behave under the influence of strong electric fields.

2.3.1 Dielectric function

If a dielectric solid is placed in an electric field $\vec{F}$ dipoles can form or reorientate themselves. The resulting macroscopic polarization of the solid is

$$\vec{P} = \varepsilon_0 \chi \vec{F} \tag{2.13}$$

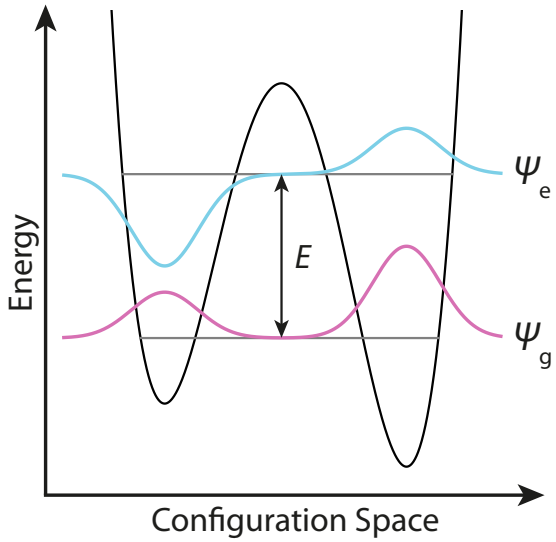

Figure 2.3: Double-well potential with the two wavefunctions of the ground state Ψ_g and the excited state Ψ_e which are separated by the energy splitting E. Adapted from [Fre21].

where ε_0 is the electric constant and χ the electric susceptibility. Generally, χ is a tensor but for amorphous solids χ is a scalar due to their isotropy. The displacement field

$$\vec{D} = \varepsilon_0 \vec{F} + \vec{P} = \varepsilon_0(1+\chi)\vec{F} = \varepsilon \vec{F} \tag{2.14}$$

allows us to introduce the dielectric function

$$\varepsilon = \varepsilon_0(1+\chi) \quad . \tag{2.15}$$

For alternating electric fields with the angular frequency ω the dielectric function can be expressed as a complex function

$$\varepsilon(\omega) = \varepsilon'(\omega) + \mathrm{i}\varepsilon''(\omega) \quad . \tag{2.16}$$

The real part ε' contains energy storing processes which occur in phase with the electric field whereas the imaginary part ε'' contains dissipative processes which are phase-shifted by 90°. Different effects contribute to the dielectric function depending on the frequency of the applied electric field. The measurements in this thesis were performed at frequencies near $f \approx 1\,\mathrm{GHz}$ so that only reorientating dipoles need to be considered while ionic and electronic contributions can be assumed to be constant [Hun23].
The dielectric loss with the loss angle δ quantifies how much electromagnetic energy is dissipated in the dielectric solid and can be expressed as the ratio of the imaginary and real part of the dielectric function

$$\tan\delta = \frac{\varepsilon''}{\varepsilon'} \quad . \tag{2.17}$$

2.3.2 Interaction of a two-level system with an electric field

A two-level system has a dipole moment $\vec{p}$ if the tunneling object has an electric charge. This dipole moment can couple to an external electric field $\vec{F}$ which causes the tunneling parameters Δ and Δ_0 to change. This change can be considered by adding a perturbation Hamiltonian $\hat{H}_{\mathrm{pert}}$ to the unperturbed Hamiltonian $\hat{H}$ from equation 2.8 if small field strengths and therefore small variations in Δ and Δ_0 are assumed. In the basis of the uncoupled states $\{\psi_{\mathrm{a}}, \psi_{\mathrm{b}}\}$ one can write

$$\hat{H}_{\mathrm{tot}} = \hat{H} + \hat{H}_{\mathrm{pert}} \tag{2.18}$$

$$\hat{H}_{\mathrm{pert}} = \frac{1}{2}\begin{pmatrix} \delta\Delta & -\delta\Delta_0 \\ -\delta\Delta_0 & -\delta\Delta \end{pmatrix} \approx \frac{1}{2}\begin{pmatrix} \delta\Delta & 0 \\ 0 & -\delta\Delta \end{pmatrix} \quad . \tag{2.19}$$

In the second step of equation 2.19 it was assumed that the barrier height V and the well distance d are only weakly affected by the applied electric field. Therefore, it can be assumed that the variations of the coupling energy $\delta\Delta_0$ are much smaller than the variations of the asymmetry energy $\delta\Delta$. These assumptions could be confirmed experimentally in [Phi81, Lis15, Sar16]. Using the rotation matrices from equation 2.9 the perturbation Hamiltonian can be transformed into the basis of the coupled states $\{\Psi_{\mathrm{g}}, \Psi_{\mathrm{e}}\}$ so that we obtain

$$\hat{\mathcal{H}}_{\mathrm{pert}} = \hat{R}_\phi \hat{H}_{\mathrm{pert}} \hat{R}_\phi^{-1} = \frac{1}{2E}\begin{pmatrix} \Delta & \Delta_0 \\ \Delta_0 & -\Delta \end{pmatrix} \delta\Delta \quad . \tag{2.20}$$

The change of the asymmetry energy can be expressed as

$$\delta\Delta = 2\vec{p}\vec{F} = 2pF_{\mathrm{ac}} \cos(\omega t)\cos(\theta) \tag{2.21}$$

where $F_{\mathrm{ac}}(t) = F_{\mathrm{ac}}\cos(\omega t)$ is the applied alternating electric field with the angular frequency ω and the amplitude F_{ac}, and θ is the the angle between the dipole moment $\vec{p}$ and the electric field $\vec{F}$. The total Hamiltonian in the basis of the coupled states is then

$$\hat{\mathcal{H}}_{\mathrm{tot}} = \hat{\mathcal{H}} + \hat{\mathcal{H}}_{\mathrm{pert}} = \frac{1}{2}\begin{pmatrix} E & 0 \\ 0 & -E \end{pmatrix} + \frac{1}{E}\begin{pmatrix} \Delta & \Delta_0 \\ \Delta_0 & -\Delta \end{pmatrix} pF_{\mathrm{ac}}\cos(\omega t)\cos(\theta) \quad . \tag{2.22}$$

The variation of the energy splitting is the difference of the diagonal elements of the perturbation Hamiltonian:

$$\delta E = \frac{2\Delta}{E} pF_{\mathrm{ac}}\cos(\omega t)\cos(\theta) \quad . \tag{2.23}$$

The perturbation Hamiltonian also has off-diagonal elements which couple the states of the two wells $|\Psi_{\mathrm{g}}\rangle$ and $|\Psi_{\mathrm{e}}\rangle$ so that transitions between them can be induced by the applied electric field.

2.3.3 Relaxation processes

An alternating electric field modulates the energy splitting of a tunneling system according to equation 2.23. This leads to a periodic variation of the occupation number difference between the excited and ground state $\delta(\Delta n)$. In this manner also the polarization of the tunneling system is modulated. If one assumes the electric field to be small ($\vec{F} \cdot \vec{p} \ll k_\mathrm{B}T$) the variation of the polarization can be written as

$$\delta P = \delta(\Delta n) p \cos(\theta) \frac{\Delta}{E} \quad . \tag{2.24}$$

The occupation number difference at thermal equilibrium can be calculated as

$$\Delta n = \frac{\Delta N}{N} = \tanh\left(\frac{E}{2k_\mathrm{B}T}\right) \tag{2.25}$$

according to [Ens05]. The rate of the polarization of the tunneling system $P(t)$ to relax back to its equilibrium value $P_0(t)$ can be calculated using the Debye formalism [Deb13]. The rate can be expressed as

$$\frac{\mathrm{d}P(t)}{\mathrm{d}t} = -\frac{P(t) - P_0(t)}{\tau_1} \tag{2.26}$$

where τ_1 is the relaxation time. By using equation 2.13 the dielectric susceptibility can be calculated as

$$\chi(\omega) = \frac{\chi(\omega = 0)}{1 - \mathrm{i}\omega\tau_1} \quad . \tag{2.27}$$

The static dielectric susceptibility $\chi(\omega = 0)$ can be determined by using the partial derivatives of the equations 2.13, 2.23, 2.24 and 2.25 so that we receive

$$\chi(0) = \frac{1}{\varepsilon_0}\frac{\partial P}{\partial F} = \frac{1}{\varepsilon_0}\frac{\partial(\delta P)}{\partial(\Delta n)}\frac{\partial(\Delta n)}{\partial E}\frac{\partial E}{\partial F} = \frac{p^2\cos^2(\theta)}{\varepsilon_0 k_\mathrm{B}T}\left(\frac{\Delta}{E}\right)^2 \mathrm{sech}^2\left(\frac{E}{2k_\mathrm{B}T}\right) \quad . \tag{2.28}$$

By inserting this into equation 2.27 we can calculate the real and imaginary part of the change of the susceptibility and the dielectric function due to relaxation processes. As the susceptibility and the dielectric function only differ by a constant value according to equation 2.15 their changes are equal:

$$\delta\chi'_\mathrm{rel} = \delta\varepsilon'_\mathrm{rel} = \chi(0)\frac{1}{1 + \omega^2\tau_1^2} \tag{2.29}$$

$$\delta\chi''_\mathrm{rel} = \delta\varepsilon''_\mathrm{rel} = \chi(0)\frac{\omega\tau_1}{1 + \omega^2\tau_1^2} \quad . \tag{2.30}$$

In figure 2.4 the real and imaginary part of the dielectric function are plotted as a function of $\omega\tau_1$. For low frequencies $\omega\tau_1 \ll 1$ the dipoles are able to follow the electric

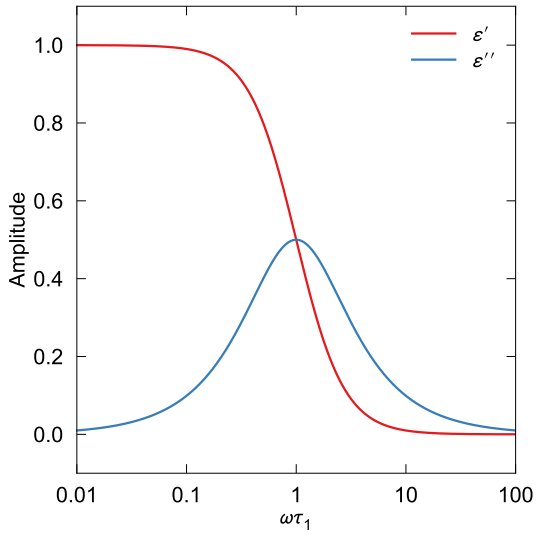

Figure 2.4: Real and imaginary part of the dielectric function for relaxational processes as a function of $\omega\tau_1$. τ_1 is the relaxation time.

field and energy is stored so that the real part is large. For increasing frequencies the dipoles follow the electric field more and more delayed so that the real part declines and the imaginary part increases until it reaches a maximum at $\omega\tau_1 = 1$. For even higher frequencies $\omega\tau_1 \gg 1$ the electric field changes so quickly that the dipoles are not able to follow the electric field and the real and imaginary part vanish.
The measurements in this thesis were performed at a temperature of $T = 30\,\mathrm{mK}$ so that the dominant relaxation process of a tunneling system is the emission or absorption of a single thermal phonon. The one-phonon relaxation rate can be calculated as

$$\tau_{1,\mathrm{ph}}^{-1} = \frac{1}{2\pi\rho\hbar^4}\left(\frac{\gamma_\mathrm{l}^2}{v_\mathrm{l}^5} + 2\frac{\gamma_\mathrm{t}^2}{v_\mathrm{t}^5}\right)\left(\frac{\Delta_0}{E}\right)^2 E^3 \coth\left(\frac{E}{2k_\mathrm{B}T}\right) \tag{2.31}$$

according to [Jä72] where ρ is the mass density, γ_l and γ_t are the coupling strengths of the longitudinal and transversal phonons and v_l and v_t are the longitudinal and transversal sound velocities.

2.3.4 Resonant processes

In the previous section we saw that relaxational processes need thermal phonons which the tunneling system can absorb or emit to relax back to its equilibrium state. Resonant processes on the other hand occur when the energy splitting E of a tunneling system equals the photon energy of the applied electric field
$E = \hbar\omega_\mathrm{TS} = \hbar\omega$. At low temperatures it is more likely that a tunneling system is in its ground state so that it can absorb a photon resonantly and thus is excited. At higher temperatures it is more likely for a tunneling system to be in its excited state

due to thermal excitation. An excited tunneling system can return to its ground state by emitting an additional photon (stimulated emission). For $T \to \infty$ the probability for a tunneling system to be in its ground or excited state is equal so that the effects of stimulated emission and resonant absorption cancel each other out. The contribution of resonant processes to the dielectric function were determined by Carruzo *et al.* [Car94]. Their results are

$$\delta\chi'_{\mathrm{res}} = \delta\varepsilon'_{\mathrm{res}} = \frac{p^2\cos^2(\theta)}{\varepsilon_0\hbar}\left(\frac{\Delta_0}{E}\right)^2 \tanh\left(\frac{E}{2k_{\mathrm{B}}T}\right) b'(\omega) \tag{2.32}$$

$$\delta\chi''_{\mathrm{res}} = \delta\varepsilon''_{\mathrm{res}} = \frac{p^2\cos^2(\theta)}{\varepsilon_0\hbar}\left(\frac{\Delta_0}{E}\right)^2 \tanh\left(\frac{E}{2k_{\mathrm{B}}T}\right) b''(\omega) \tag{2.33}$$

with

$$b'(\omega) = \frac{(\omega+\omega_{\mathrm{TS}})\tau_2^2}{(\omega+\omega_{\mathrm{TS}})\tau_2^2+1} - \frac{(\omega-\omega_{\mathrm{TS}})\tau_2^2}{(\omega-\omega_{\mathrm{TS}})\tau_2^2+1} \tag{2.34}$$

$$b''(\omega) = \frac{\tau_2}{(\omega-\omega_{\mathrm{TS}})\tau_2^2+1} - \frac{\tau_2}{(\omega+\omega_{\mathrm{TS}})\tau_2^2+1} \tag{2.35}$$

where τ_2 is the transversal relaxation time. The frequency dependencies (equations 2.34 and 2.35) are depicted in figure 2.5 as a function of $\omega/\omega_{\mathrm{TS}}$. For $\omega \ll \omega_{\mathrm{TS}}$ the tunneling system is able to follow the electric field so that the real part contributes to the dielectric function whereas the imaginary part vanishes. As the frequency of the applied electric field gets closer to the resonance frequency ω_{TS} the real and imaginary part increase because the photon absorption rate increases. At the resonance frequency the photon absorption rate and thus the imaginary part are maximal whereas the real part undergoes a sign change. For even higher frequencies $\omega \gg \omega_{\mathrm{TS}}$ both real and imaginary parts vanish as the tunneling system is not able to follow the driving field.

2.3.5 Parameter distribution

Until now we have only looked at a single tunneling system. However, in an amorphous solid there are many tunneling systems with different tunneling parameters so we have to take into account a distribution of the parameters Δ and λ. In the standard tunneling model Anderson *et al.* [And72] and Phillips [Phi72] assumed that Δ and λ are independent from each other and uniformly distributed so that the distribution function can be expressed as

$$P(\Delta,\lambda)\mathrm{d}\Delta\mathrm{d}\lambda = P_0\mathrm{d}\Delta\mathrm{d}\lambda \tag{2.36}$$

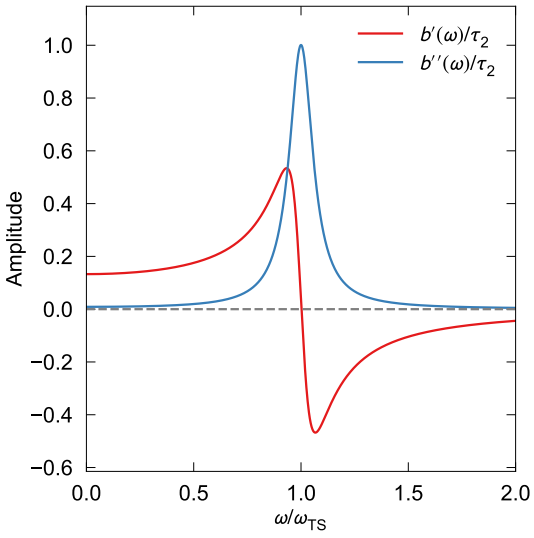

Figure 2.5: Real and imaginary part of the dielectric function in terms of $\omega/\omega_{\mathrm{TS}}$ for resonant processes. τ_2^{-1} is the transversal relaxation rate and the width of the Lorentzian line shaped imaginary part.

where P_0 is a constant material dependent parameter. For further calculations it is useful to perform a variable transformation of the distribution function:

$$P(E,\Delta_0)\mathrm{d}E\mathrm{d}\Delta_0 = P(\Delta,\lambda)\left|\frac{\partial\lambda}{\partial\Delta_0}\right|\left|\frac{\partial\Delta}{\partial E}\right|\mathrm{d}E\mathrm{d}\Delta_0 = \frac{P_0}{\Delta_0}\frac{E}{\sqrt{E^2-\Delta_0^2}}\mathrm{d}E\mathrm{d}\Delta_0 \quad . \tag{2.37}$$

This expression will be used in section 2.4.1 to calculate the dielectric loss $\tan\delta$ under the influence of an electric bias field. Figure 2.6 shows the distribution function (equation 2.37) as a function of $\frac{\Delta_0}{E}$. Only the singularity at $\Delta_0 = E$ is integrable. The singularity at $\Delta_0 = 0$ is not integrable and for $\Delta_0 \to 0$ the double well becomes increasingly asymmetric. To assure an integrable parameter distribution a minimal tunneling splitting has to be chosen. Tunneling splittings below that minimal tunneling splitting correspond to such an asymmetric double well potential that the potential can be handled as a single-well potential because of a negligibly small probability for the tunneling object to be in the upper well. Luck [Luc16] suggested a minimal tunneling splitting of $\Delta_{0,\mathrm{min}} \approx 10^{-3} k_{\mathrm{B}} T_{\mathrm{min}}$ to be sufficient where T_{min} is the lowest temperature at which the measurements have been performed.

In order to determine the relaxational and resonant contributions to the dielectric function for all tunneling systems in an amorphous solid the relaxational (equation 2.29 and 2.30) and resonant contributions (equation 2.32 and 2.33) have to be integrated over all possible energies and tunneling splittings using the distribution function from equation 2.37. For the dipole moment $\vec{p}^{\,2} = p^2\cos^2(\theta)$ the average of all dipole moment directions

$$\langle\vec{p}^{\,2}\rangle = \frac{\int_0^{2\pi}\mathrm{d}\phi\int_0^{\pi}\mathrm{d}\theta\sin(\theta)p^2\cos^2(\theta)}{\int_0^{2\pi}\mathrm{d}\phi\int_0^{\pi}\mathrm{d}\theta\sin(\theta)} = \frac{p^2}{3} \tag{2.38}$$

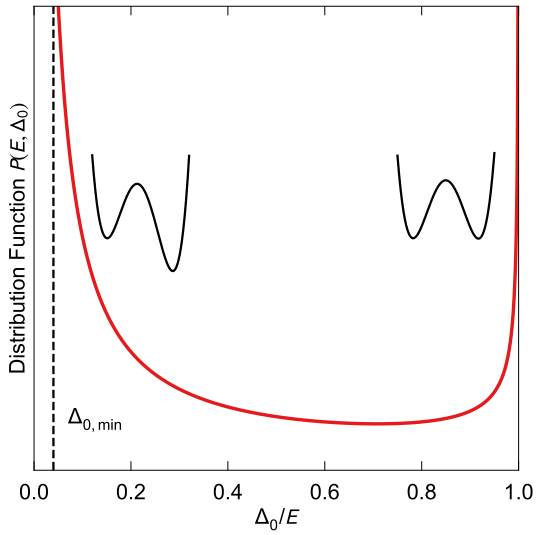

Figure 2.6: Distribution function $P(E, \Delta_0)$ as a function of $\frac{\Delta_0}{E}$. For $\Delta_0 \to 0$ the two-level systems become increasingly asymmetric whereas for $\Delta_0 \to E$ the two-level systems become more and more symmetric. Below the minimal tunneling splitting $\Delta_{0,\min}$ the probability for the tunneling object to be in the upper well is so small that the potential can be handled as a single well. Adapted from [Sei18].

is used. The integrals of the dielectric function

$$\frac{\delta\varepsilon'}{\varepsilon'} = \int_{\Delta_{0,\min}}^{E_{\max}} \mathrm{d}E \int_{\Delta_{0,\min}}^{E} \mathrm{d}\Delta_0 \left(\frac{\delta\varepsilon'_{\mathrm{rel}}}{\varepsilon'} + \frac{\delta\varepsilon'_{\mathrm{res}}}{\varepsilon'} \right) P(E, \Delta_0) \tag{2.39}$$

$$\frac{\delta\varepsilon''}{\varepsilon'} = \int_{\Delta_{0,\min}}^{E_{\max}} \mathrm{d}E \int_{\Delta_{0,\min}}^{E} \mathrm{d}\Delta_0 \left(\frac{\delta\varepsilon''_{\mathrm{rel}}}{\varepsilon'} + \frac{\delta\varepsilon''_{\mathrm{res}}}{\varepsilon'} \right) P(E, \Delta_0) \tag{2.40}$$

have to be solved numerically.
The relative changes of the real and imaginary part of the dielectric function are depicted in figure 2.7 in terms of the temperature. The relaxational and resonant contributions are shown separately as well as the sum of them.

Relaxational contribution

At low temperatures $T < 1\mathrm{K}$ no phonons exist and the relaxation times are too long so that relaxational processes do not contribute to the dielectric function. For higher temperatures $T \gtrsim 1\mathrm{K}$ both real and imaginary part increase since the number of phonons increases and the relaxation times become shorter. While the real part increases monotonously the imaginary part reaches a plateau for increasing temperatures. The reason for this is that only tunneling systems with $\omega\tau_1 \approx 1$ contribute to the imaginary part of the dielectric function (see figure 2.4).

Resonant contribution

Only tunneling systems with energy splittings $E = \hbar\omega_{\mathrm{TS}} > k_{\mathrm{B}}T$ are in their ground state and can thus contribute resonantly to the dielectric function. At high temperatures this condition only applies for tunneling systems with large energy splittings

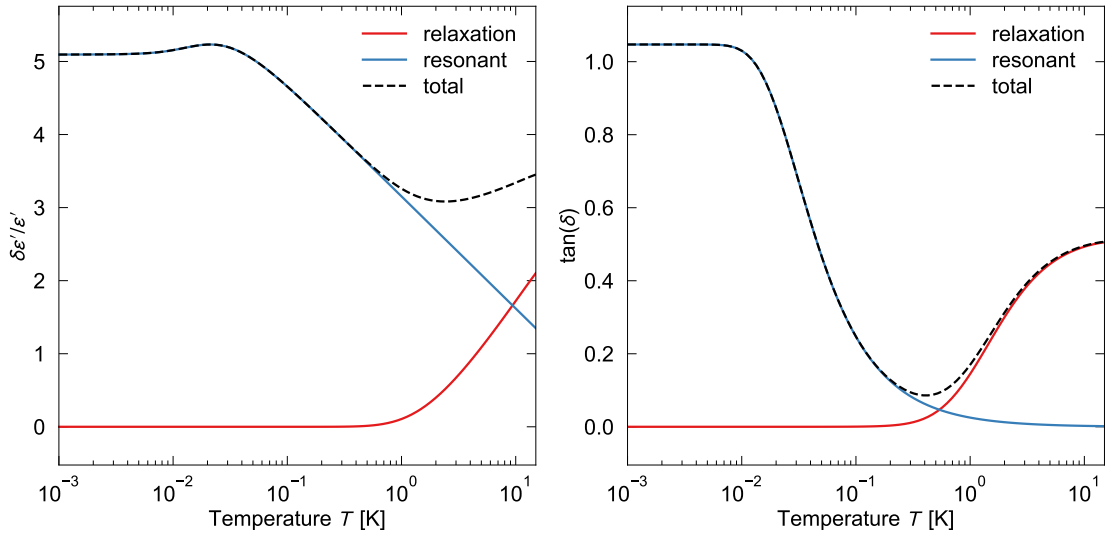

Figure 2.7: Relative change of the real (left) and imaginary part (right) of the dielectric function as a function of the temperature at an excitation frequency of $f = 1\,\mathrm{GHz}$. The dielectric loss equals the relative change of the imaginary part of the dielectric function $\tan\delta = \frac{\delta\varepsilon''}{\varepsilon'}$.

so that only tunneling systems with $\omega_{\mathrm{TS}} \gg \omega$ are able to contribute to the dielectric function. As can be seen in figure 2.5, the real part of the dielectric function approaches a small constant value for $\omega_{\mathrm{TS}} \gg \omega$. Therefore, the real part only contributes to a small extent to the dielectric loss at high temperatures. For decreasing temperatures the number of tunneling systems which are thermally excited decreases. Therefore, also tunneling systems with lower energy splittings are able to contribute to the real part leading to an increasing contribution to the dielectric function. For lower temperatures also tunneling systems at resonance $\omega_{\mathrm{TS}} \approx \omega$ are able to contribute to the dielectric function. As can be seen in figure 2.5, the real part undergoes a sign change at resonance leading to a small maximum of the contribution to the dielectric function at $T \approx 20\mathrm{mK}$. For even lower temperatures also tunneling systems on the other side of the resonance $\omega_{\mathrm{TS}} \ll \omega$ are able to contribute to the dielectric function. However, these additional tunneling systems do not lead to an increase of the contribution because the real part vanishes for $\omega_{\mathrm{TS}} \ll \omega$ as can be seen in figure 2.5. Therefore, the contribution to the dielectric function reaches a plateau at lowest temperatures.

As can be seen in figure 2.5, only tunneling systems at resonance $\omega_{\mathrm{TS}} \approx \omega$ contribute to the imaginary part of the dielectric function. At high temperatures only tunneling systems with large energy splittings $\omega_{\mathrm{TS}} \gg \omega$ are in their ground state so that the contribution to the dielectric function vanishes. As the temperature decreases more and more tunneling systems are in their ground state so that they can resonantly

absorb photons leading to an increasing contribution to the dielectric function. At lowest temperatures all tunneling systems are in their ground state so that all of them being around the resonance frequency $\omega_{\mathrm{TS}} \approx \omega$ are able to contribute to the dielectric function resulting in the contribution to reach a plateau.

2.3.6 Saturation by large electric fields

Increasing the intensity of the applied electric field increases the number of photons which interact resonantly with the tunneling systems. When the interaction rate exceeds the relaxation rate τ_1^{-1} of an already excited tunneling system it interacts with a photon by stimulated emission, i.e. by emitting a coherent photon and returning to its ground state. The dielectric loss decreases for increasing electric fields because resonant absorption and stimulated emission cancel each other out at high electric fields so that the tunneling systems are saturated. Hunklinger and Arnold [Hun76] determined a formula for the saturation loss

$$\tan\delta = \frac{\pi P_0 p^2}{3\varepsilon_0\varepsilon_{\mathrm{r}}} \tanh\left(\frac{\hbar\omega}{2k_{\mathrm{B}}T}\right) \frac{1}{\sqrt{1+\left(\frac{F_{\mathrm{ac}}}{F_{\mathrm{c}}}\right)^2}} \tag{2.41}$$

where ε_{r} is the relative permittivity and

$$F_{\mathrm{c}} = \frac{3\hbar}{2p}\frac{1}{\tau} \tag{2.42}$$

is the critical field strength at which the tunneling systems begin to saturate. Here p is the average dipole moment and

$$\tau = \sqrt{\tau_{1,\min}\tau_2} \tag{2.43}$$

is the characteristic lifetime of a tunneling system's excited state, in the following shortened named as lifetime of a tunneling system. The dielectric loss is independent of the electric field at low field strengths $F_{\mathrm{ac}} \ll F_{\mathrm{c}}$ which allows us to define the field independent low power loss

$$\tan\delta_0 = \frac{\pi P_0 p^2}{3\varepsilon_0\varepsilon_{\mathrm{r}}} \tanh\left(\frac{\hbar\omega}{2k_{\mathrm{B}}T}\right) \quad . \tag{2.44}$$

The normalized dielectric loss $\tan\delta/\tan\delta_0$ is depicted in figure 2.8 as a function of the field strength F_{ac}.

2.4 Non-equilibrium loss and Landau-Zener transitions

This section deals with the non-equilibrium loss of tunneling systems. Equation 2.21 shows that electric fields modulate the asymmetry energy of tunneling systems

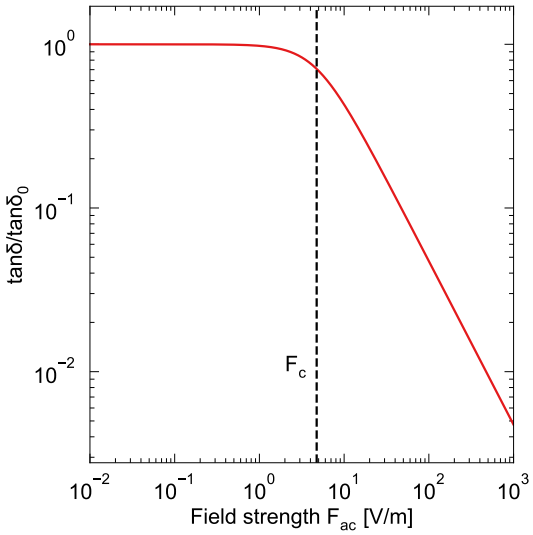

Figure 2.8: Normalized dielectric loss $\tan\delta/\tan\delta_0$ as a function of the field strength F_{ac}. The dashed line marks the critical field strength F_{c} from equation 2.42. The used parameters are $p = 1\,\mathrm{D}$ and $\tau = 10\,\mu\mathrm{s}$.

which leads to a modulation of the energy splitting. In this section we consider tunneling systems in an electric bias field with the field strength $\vec{F}_{\mathrm{b}}$ which modifies the asymmetry energy by

$$\delta\Delta(t) = 2\vec{p}\vec{F}_{\mathrm{b}}(t) \tag{2.45}$$

and therefore changes the energy splitting

$$E(t) = \sqrt{\Delta_0^2 + (\Delta + \delta\Delta(t))^2} \quad . \tag{2.46}$$

Furthermore, we assume that the driving field F_{ac} is weak compared to the bias field F_{b} so that its influence on the modulation of the energy splitting is negligibly small. At low temperatures only tunneling systems which absorb photons resonantly ($\omega_{\mathrm{TS}} \approx \omega$) contribute to the imaginary part of the dielectric function. Therefore, only tunneling systems at resonance have to be considered and the energy splitting can be expanded around $\delta\Delta = 0$. The constant and linear terms of the taylor expansion of equation 2.46 are sufficient:

$$E(t) \approx E_0 + \sqrt{1 - \left(\frac{\Delta_0}{E_0}\right)^2}\,\delta\Delta(t) \quad . \tag{2.47}$$

Here $E_0 = \sqrt{\Delta_0^2 + \Delta^2}$ was used. According to Burin *et al.* [Bur13] and Khalil [Kha13] the energy bias rate can be defined as

$$\nu = \frac{1}{\hbar}\frac{\mathrm{d}E(t)}{\mathrm{d}t} = \frac{1}{\hbar}\sqrt{1 - \left(\frac{\Delta_0}{E_0}\right)^2}\,2p\dot{F}_{\mathrm{b}}\cos(\vartheta) \tag{2.48}$$

where ϑ is the angle between the dipole moment $\vec{p}$ and the bias field $\vec{F}_\mathrm{b}$. If the bias rate $\dot{F}_\mathrm{b}$ is constant the energy splitting is linear in time and can be written as

$$E(t) = \hbar\omega + \hbar\nu(t - t_0) \quad . \tag{2.49}$$

For a time dependent energy splitting the wave function of the tunneling system is also time dependent and can be written as

$$|\Psi(t)\rangle = c_\mathrm{g}(t)\,|\Psi_\mathrm{g}\rangle + c_\mathrm{e}(t)\,|\Psi_\mathrm{e}\rangle \quad . \tag{2.50}$$

The coefficients $c_\mathrm{g}(t)$ and $c_\mathrm{e}(t)$ can be obtained by solving the time dependent Schrödinger equation

$$\mathrm{i}\hbar\frac{\partial}{\partial t}\,|\Psi(t)\rangle = \hat{\mathcal{H}}_\mathrm{tot}\,|\Psi(t)\rangle \tag{2.51}$$

where $\hat{\mathcal{H}}_\mathrm{tot}$ is the Hamiltonian from equation 2.22. By assuming that relaxation processes do not occur during resonant crossings and that the driving field does not effect the energy splitting $\frac{\Delta}{E}pF_\mathrm{ac} \ll \frac{E}{2}$ we obtain

$$\mathrm{i}\hbar\dot{c}_\mathrm{e}(t) = \frac{E}{2}c_\mathrm{e}(t) + \hbar\Omega_\mathrm{R}\cos(\omega t)c_\mathrm{g}(t) \tag{2.52}$$

$$\mathrm{i}\hbar\dot{c}_\mathrm{g}(t) = -\frac{E}{2}c_\mathrm{g}(t) + \hbar\Omega_\mathrm{R}\cos(\omega t)c_\mathrm{e}(t) \tag{2.53}$$

where Ω_R is the Rabi frequency at which a tunneling system oscillates between ground and excited state in the presence of the driving field F_ac

$$\Omega_\mathrm{R} = \frac{\Delta_0}{E}\frac{pF_\mathrm{ac}}{\hbar}\cos(\theta) = \frac{\Delta_0}{E}\Omega_\mathrm{R0}\cos(\theta) \quad . \tag{2.54}$$

By transforming the differential equations 2.52 and 2.53 into a rotating frame with

$$\begin{pmatrix} a_\mathrm{e}(t) \\ a_\mathrm{g}(t) \end{pmatrix} = \begin{pmatrix} c_\mathrm{e}(t)e^{\frac{\mathrm{i}\omega t}{2}} \\ c_\mathrm{g}(t)e^{-\frac{\mathrm{i}\omega t}{2}} \end{pmatrix} \tag{2.55}$$

we obtain the new differential equations

$$\dot{a}_\mathrm{e}(t) = -\frac{\mathrm{i}\nu}{2}(t - t_0)a_\mathrm{e} - \frac{\mathrm{i}\Omega_\mathrm{R}}{2}a_\mathrm{g} \tag{2.56}$$

$$\dot{a}_\mathrm{g}(t) = \frac{\mathrm{i}\nu}{2}(t - t_0)a_\mathrm{g} - \frac{\mathrm{i}\Omega_\mathrm{R}}{2}a_\mathrm{e} \tag{2.57}$$

where we neglected all terms which oscillate at $2\omega t$ using the rotating wave approximation. These equations are formally equivalent to the equations of the Landau-Zener problem of a two-level system [Lan32, Zen32, Stü32, Maj32]. As it is difficult to access these publications we refer to [Iva22] where these works are summarized in detail.

2.4.1 Single ramp biasing

Now we look at transitions of tunneling systems in the limit of slow and fast bias rates for a single bias ramp, i.e. a ramp of length t_b and amplitude F_b with a constant rate of change $\dot{F}_\mathrm{b} = F_\mathrm{b}/t_\mathrm{b}$. A sketch of a Landau-Zener scenario can be seen in figure 2.9. The bias field leads to a change the energy splitting (left). When the energy splitting matches the photon energy of the driving field a photon can be absorbed resonantly (center) so that one can lower the energy of the upper level by the photon energy. This leads to an avoided level crossing (right). At slow energy bias rates $\nu \ll \Omega_\mathrm{R}^2$ an adiabatic transition can occur in which the tunneling system absorbs a photon and thus is excited. At fast energy bias rates $\nu \gg \Omega_\mathrm{R}^2$it is more likely that the tunneling system stays in its ground state by performing a non-adiabatic Landau-Zener transition. Using the equations of the Landau-Zener problem 2.56 and 2.57 the probability for a resonant absorption can be calculated as

$$P_{\mathrm{g}\to\mathrm{e}} = |a_\mathrm{e}|^2 = 1 - P_\mathrm{LZ} = 1 - \exp(-\gamma) = 1 - \exp\left(-\frac{\pi\Omega_\mathrm{R}^2}{2\nu}\right) \tag{2.58}$$

and for a Landau-Zener transition as

$$P_\mathrm{LZ} = |a_\mathrm{g}|^2 = \exp(-\gamma) \quad . \tag{2.59}$$

The next step is to calculate the dielectric loss which occurs through an adiabatic transition when a photon is absorbed resonantly by the tunneling system. Following Burin *et al.* [Bur13] and Khalil [Kha13] the dissipated energy $\mathrm{d}E_\mathrm{dis}$ is calculated by integrating over the volume V of all N tunneling systems which can absorb photons of the energy $\hbar\omega$ with the probability $P_{\mathrm{g}\to\mathrm{e}}$:

$$\mathrm{d}E_\mathrm{dis} = \int \mathrm{d}V \int \mathrm{d}N\hbar\omega P_{\mathrm{g}\to\mathrm{e}} \quad . \tag{2.60}$$

In the next step we integrate over the distribution function $P(E, \Delta_0)$ and the energy E. For the integral over the energy it is sufficient to account for resonant tunneling systems during a time interval $\mathrm{d}t$ so that we obtain

$$\mathrm{d}E_\mathrm{dis} = \hbar\omega P_0 V \int_0^1 \mathrm{d}(\cos\theta) \int_0^{\hbar\omega} \mathrm{d}\Delta_0 \int_{\hbar\omega-\hbar\nu\mathrm{d}t}^{\hbar\omega+\hbar\nu\mathrm{d}t} \mathrm{d}E \frac{(1-e^{-\gamma})E}{\Delta_0\sqrt{E^2-\Delta_0^2}} \quad . \tag{2.61}$$

By assuming the change of the energy splitting to be small $\hbar\nu\mathrm{d}t \ll \hbar\omega$, inserting the equations 2.54 and 2.58 and substituting $x = \frac{\Delta_0}{\hbar\omega}$ the dissipated power P_dis can be calculated as

$$P_\mathrm{dis} = \frac{\mathrm{d}E_\mathrm{dis}}{\mathrm{d}t} = \pi\omega V P_0 p^2 F_\mathrm{ac}^2 \int_0^1 \mathrm{d}(\cos\theta)\cos^2\theta \int_0^1 \frac{1-e^{-\gamma}}{\gamma} \frac{x\mathrm{d}x}{\sqrt{1-x^2}} \quad . \tag{2.62}$$

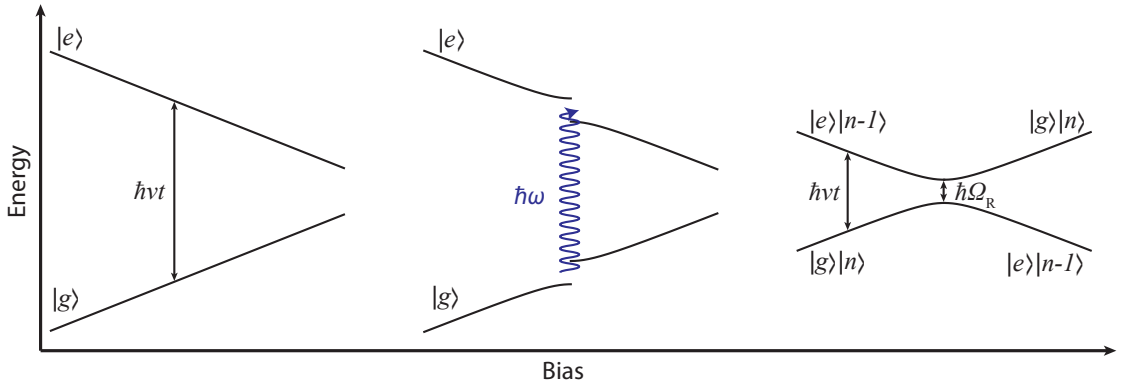

Figure 2.9: Combined picture of the energy states of the Landau-Zener problem and the photon field. The bias field changes the energy splitting (left). When the energy splitting matches the photon energy of the driving field a photon can be absorbed resonantly (center) leading to an avoided level crossing (right). Adapted from [Fre21].

The dielectric loss

$$\tan\delta = \frac{P_{\mathrm{dis}}}{\omega W_{\mathrm{tot}}} \tag{2.63}$$

is the ratio of the dissipated power per cycle and the stored energy W_{tot}. In our case we use an LC-resonator yielding the stored energy as $W_{\mathrm{tot}} = \varepsilon_0\varepsilon_{\mathrm{r}}F_{\mathrm{ac}}^2 V$ so that we obtain

$$\tan\delta = \frac{\pi P_0 p^2}{\varepsilon_0\varepsilon_{\mathrm{r}}}\int_0^1 \mathrm{d}(\cos\theta)\cos^2\theta\int_0^1 \frac{1-e^{-\gamma}}{\gamma}\frac{x\mathrm{d}x}{\sqrt{1-x^2}} \quad . \tag{2.64}$$

In the case of fast bias rates $\nu \gg \Omega_{\mathrm{R}}^2$ we can approximate $e^{-\gamma} \approx 1-\gamma$ and the evaluation of the integral yields

$$\tan\delta = \frac{\pi P_0 p^2}{3\varepsilon_0\varepsilon_{\mathrm{r}}} \tag{2.65}$$

which can be identified as the low-power loss from equation 2.44. For slower bias rates equation 2.64 has to be solved numerically. Burin *et al.* [Bur13] and Khalil [Kha13] defined the dimensionless bias rate as

$$\xi = \frac{4\hbar|\dot{F}_{\mathrm{b}}|}{\pi p F_{\mathrm{ac}}^2} = \frac{2|\nu_0|}{\pi\Omega_{\mathrm{R0}}^2} \tag{2.66}$$

where $\nu_0 = \frac{2p\dot{F}_{\mathrm{b}}}{\hbar}$. With that we obtain for the dielectric loss

$$\tan\delta = 3\tan\delta_0\xi\int_0^1 \mathrm{d}(\cos\theta)\cos\theta\int_0^1 \mathrm{d}x\frac{1}{x}\left(1-\exp\left(-\frac{\cos\theta}{\xi}\frac{x^2}{\sqrt{1-x^2}}\right)\right) \quad . \tag{2.67}$$

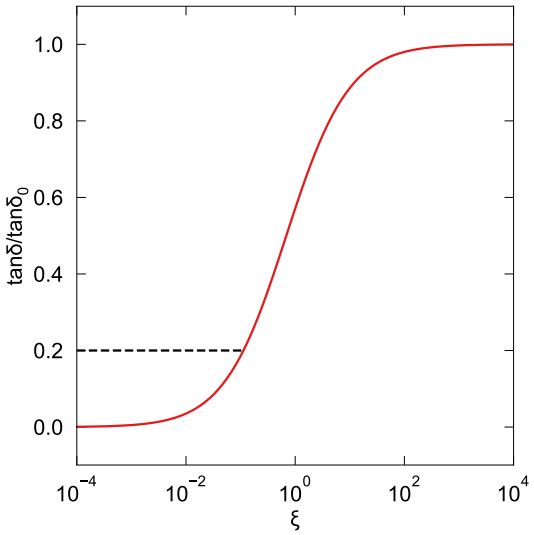

Figure 2.10: Normalized dielectric loss $\tan\delta/\tan\delta_0$ as a function of the dimensionless bias rate ξ. The curve is the result of the numerical integration of equation 2.67. The black dashed line marks the saturation limit in which relaxation processes take place during resonant transitions.

The numerical solution of the normalized dielectric loss $\tan\delta/\tan\delta_0$ is depicted in figure 2.10. At slow bias rates the dielectric loss vanishes because we assumed that in this limit relaxation processes can be neglected. However, at slow bias rates relaxation processes can take place during resonant transitions preventing the loss from approaching zero. This corresponds to the saturation limit of equation 2.41 and is marked as a black dashed line in figure 2.10. Following Burin *et al.* [Bur13] and Khalil [Kha13] the critical bias rate below which relaxation processes occur during resonant transitions is calculated as

$$\xi_1 = \frac{2}{\pi\Omega_{\mathrm{R}0}\tau} \tag{2.68}$$

where τ is the characteristic lifetime of a tunneling system from equation 2.43. For increasing bias rates an increasing number of tunneling systems perform resonant transitions leading to an increase of the dielectric loss. While at high bias rates even more tunneling systems are swept through the transition region an increasing number of them perform Landau-Zener transitions so that more tunneling systems stay in the ground state. The effects of more tunneling systems being swept through the transition region and less absorption cancel each other out which leads to the dielectric loss reaching a plateau.

2.4.2 Continuous biasing

Until now we have only considered the influence of a single bias ramp on the dielectric loss. In this section we will discuss how the dielectric loss is manipulated by a periodic bias field with the amplitude $F_{\mathrm{b}}(t) = F_{\mathrm{b}}(t + T_{\mathrm{b}})$. We choose a triangle signal as periodic signal because the absolute value of the rate of change of the triangle signal

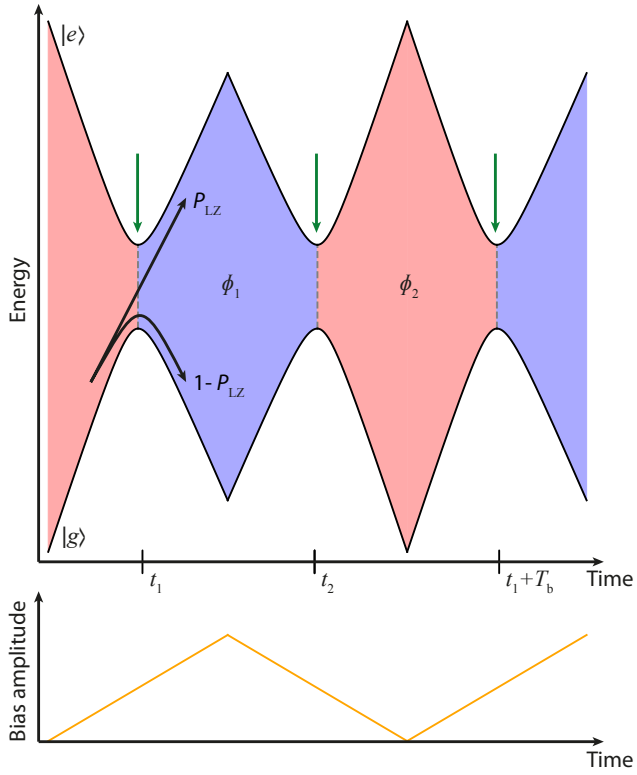

Figure 2.11: Combined picture of the energy states of the Landau-Zener problem and the photon field for a continuous triangular bias signal. The avoided crossings are marked with the green arrows. Throughout one bias period the tunneling system accumulates the phases ϕ_1 between the avoided crossings at t_1 and t_2 and ϕ_2 between the avoided crossings at t_2 and $t_1 + T_\mathrm{b}$. The corresponding bias signal is depicted at the bottom. Adapted from [Iva22].

$|\dot{F}_\mathrm{b}| = \frac{F_\mathrm{b}}{\frac{1}{2}T_\mathrm{b}}$ is constant in time. Even though a triangle signal is made up by an infinite number of frequencies we simplify the further discussion by approximating the bias frequency as the fundamental frequency of the triangle signal $f_\mathrm{b} = \frac{1}{T_\mathrm{b}}$. In that case the bias rate can be written as

$$\dot{F}_\mathrm{b} = 2F_\mathrm{b}f_\mathrm{b} = \frac{2U_\mathrm{b}f_\mathrm{b}}{d} \tag{2.69}$$

where U_b is the peak-peak voltage of the bias signal and d is the distance of the bias electrode to the ground plate.
An illustration of the time dependency of the energy splitting under the influence of a periodic bias field is depicted in figure 2.11. At the bottom the periodic bias signal is shown which leads to the modulation of the energy splitting. According to Ivakhnenko *et al.* [Iva22] a tunneling system accumulates the dynamic phases ϕ_1 between the avoided crossings at t_1 and t_2 and ϕ_2 between the avoided crossings at t_2 and $t_1 + T_\mathrm{b}$ in each period:

$$\phi_1 = \frac{1}{\hbar}\int_{t_1}^{t_2} E(t)\mathrm{d}t \quad , \quad \phi_2 = \frac{1}{\hbar}\int_{t_2}^{t_1+T_\mathrm{b}} E(t)\mathrm{d}t \quad . \tag{2.70}$$

Additionally the Stokes phase[2] ψ_s is accumulated during a transition. Depending on the phasing the transitions can interfere constructively or destructively with each other. For constructively interfering transitions the photon absorption rate is high resulting in a high probability of an adiabatic transition. Conversely, for destructively interfering transitions the photon absorption rate is low leading to a high probability of a non-adiabatic Landau-Zener transition. According to equation 2.70 the phases depend on the energy splitting $E(t)$. As the energy splitting is modulated by the bias rate $\dot{F}_\mathrm{b}$ according to equation 2.48 and 2.49 also the phases are modulated by the bias rate. Therefore, the dielectric loss depends on the bias frequency as well as the bias field strength as can be deduced from equation 2.70. This is in contrast to the single bias ramp of the previous section where the dielectric loss was only influenced by the bias rate and not the bias field strength and frequency explicitly. In the following part we will discuss how the dielectric loss is changed if the bias frequency or the bias field strength are varied. First we will examine the case of keeping the bias field strength constant and varying the bias frequency.
For small bias frequencies f_b, i.e. if the bias period is much longer than the relaxation time of a tunneling system $T_\mathrm{b} \gg \tau_1$, the tunneling system has the time to relax back to its ground state after each transition so that every bias period can be considered as individual and we observe the same behavior as for a single bias ramp.
For large bias frequencies f_b, i.e. for small bias periods $T_\mathrm{b} \ll \tau_1$, successive transitions interfere with each other. Although the relaxation time τ_1 is much longer than the bias period T_b tunneling systems can still relax back to their ground state after completing $m = \tau_1/T_\mathrm{b}$ coherent transitions. For that Matityahu *et al.* [Mat19] introduced a second critical bias rate

$$\xi_2 = \frac{T_\mathrm{b}}{\tau_1}\xi = \frac{8pF_\mathrm{b}}{\pi\hbar\Omega_{\mathrm{R}0}^2\tau_1} \quad . \tag{2.71}$$

For $\xi \ll \xi_2$ the single ramp limit of section 2.4.1 is valid and for $\xi \gg \xi_2$ one speaks of the continuous or coherent regime. In this regime the number of transitions which interfere constructively with each other decreases for increasing bias frequencies so that the total photon absorption rate and the dielectric loss are also decreased.
Blickberndt [Bli22] showed that for the highest bias rates the dielectric loss drops back to the same saturation limit at which relaxation processes at slowest bias rates occur during resonant transitions. The reason for that is that only tunneling systems which sit symmetrically around the resonant crossing contribute to the dielectric loss for such large bias rates. For that a third critical bias rate is introduced

$$\xi_3 = \frac{F_\mathrm{b}^2}{F_\mathrm{ac}^2} \tag{2.72}$$

[2] $\psi_\mathrm{s} = \frac{\pi}{4} + \arg\Gamma\left(1 - \frac{\mathrm{i}\gamma}{2\pi}\right) + \frac{\gamma}{2\pi}\left(\ln\left(\frac{\gamma}{2\pi}\right) - 1\right)$

which marks the bias rate at which the loss returns back to the saturation limit. Now we will also examine what happens if the bias frequency is held constant and the bias field strength, i.e. the bias amplitude, is changed. Increasing the bias amplitude results in more tunneling systems being able to absorb photons resonantly as can be seen in equation 2.45. For $\xi \ll \xi_2$ we again have the single ramp limit of section 2.4.1. In the case of $\xi \gg \xi_2$ more tunneling systems perform avoided crossings whereas the fraction of constructively interfering transitions stays constant. Increasing the bias amplitude thus causes the photon absorption rate and the dielectric loss to start increasing at higher bias rates.

3. Experimental Methods

This chapter contains the information about the experimental methods which were used in this thesis. First, we will give a brief overview of taking measurements at low temperatures. After that the radio frequency setup is introduced which is used to read out the dielectric response of the glass sample. Subsequently the properties of the glass sample and the resonator are presented. We end this chapter with an overview of the measurement principle which is needed to extract the dielectric function of the sample from the output of the resonator.

3.1 Measurements at low temperatures

In this thesis tunneling systems are modified by a continuous electric bias field. For that a sufficient amount of tunneling systems has to be in the ground state so that they are able to absorb photons resonantly. In figure 2.7 we can see that resonant interactions of tunneling systems with electric fields only take place at low temperatures because in this temperature regime the most tunneling systems are in the ground state. Equation 2.25 quantifies which fraction of tunneling systems is in the ground state and which fraction is in the excited state. The measurements were conducted at a temperature of $T = 30\,\mathrm{mK}$ and at a driving field frequency of $f = 1.125\,\mathrm{GHz}$ so that the occupation number difference between ground and excited state is $\Delta n = \tanh\left(\frac{hf}{2k_\mathrm{B}T}\right) \approx 0.72$. Using the relations $\Delta n = n_\mathrm{g} - n_\mathrm{e}$ and $n_\mathrm{g} + n_\mathrm{e} = 1$ we can conclude that a fraction of $n_g \approx 86\,\%$ of the tunneling systems are in the ground state, which is sufficient.
The setup that ensures such low temperatures is a ^{3}He/^{4}He dilution refrigerator. Information about the functionality of a ^{3}He/^{4}He dilution refrigerator can be found in [Fro92, Ens05, Pob07]. The resonator is thermally coupled to the mixing chamber of the cryostat and a carbon resistor thermometer close to the resonator is used to measure the temperature of the sample and is read out via an AC-resistance bridge[1]. Possible heat leaks can lead to unwanted and uncontrollable increases in temperature inside the cryostat. Therefore, a PID feedback-controller is used to control a heater which ensures a stable temperature.

[1] AVS-47, RV-Elektroniikka Oy Picowatt, Veromiehentie 14, FI-01510 Vantaa, Finland

3.2 Setup for measuring the dielectric response

The readout setup is shown schematically in figure 3.1. A vector network analyzer[2] (VNA) provides a radio frequency (rf) signal which is attenuated by three attenuators before entering the cryostat. The first and second attenuator attenuate the signal by 20 dB and 10 dB respectively so that standing waves in the coaxial cable, which could occur because of impedance mismatches, are suppressed. The third attenuator provides an attenuation between 0 and 81dB which can be varied in steps of 1 dB by a LabView[3] program on a computer. Then the attenuated signal enters the cryostat where a DC block filters out the DC component of the signal. After that the signal is attenuated by 20 dB before entering a heatsink which ensures a thermalization to the desired temperature in the cryostat so that less heat flows from outside the cryostat into the experiment. The following attenuation of 10 dB reduces the room temperature thermal noise so that the signal can then enter the resonator. After leaving the resonator the signal is attenuated by 3 dB before entering a heatsink. Then the signal is amplified by 20 dB by a low temperature amplifier. The following DC block filters out DC components coming from the VNA. Then the signal leaves the cryostat and is amplified by 50 dB by an rf-amplifier before it enters the VNA. The VNA is connected to a computer where the readout is analyzed in a LabView program. This programm also controls the signal generator which provides the bias signal that enters the cryostat through a heatsink. Inside the cryostat the bias signal is applied by an electrode attached to the resonator.

3.3 Resonator and sample

The resonator which has been used in this thesis was designed by [Stä24] with the software Cadence[4] and is schematically shown in figure 3.2. To allow for a good thermal coupling of the resonator to the mixing chamber of the cryostat the resonator is put into a copper box and thermally coupled to it with vacuum grease. The box is thermally well coupled to the mixing chamber due to the high thermal conductivity of the tempered oxygen-free copper. The inside of the box is sputter deposited with niobium to reduce radiation losses. To avoid ohmic losses which would heat the sample and reduce the internal quality factor of the resonator the microstructure is made of niobium which is superconducting for temperatures below $T = 9.25\,\mathrm{K}$ [Hun23]. The LC-resonator consists of an interdigital capacitor (IDC) and a mean-

[2] R&S®ZNB8, Rohde & Schwarz GmbH & Co. KG, Mühldorfstraße 15, 81671 München, Germany

[3] LabView 8.5, National Instruments Corporation, 11500 N MoPax Expwy, Austin TX 78759-3504, USA

[4] Cadence Design Systems, 21 Oak Hill Ave, Endicott, NY 13760, USA

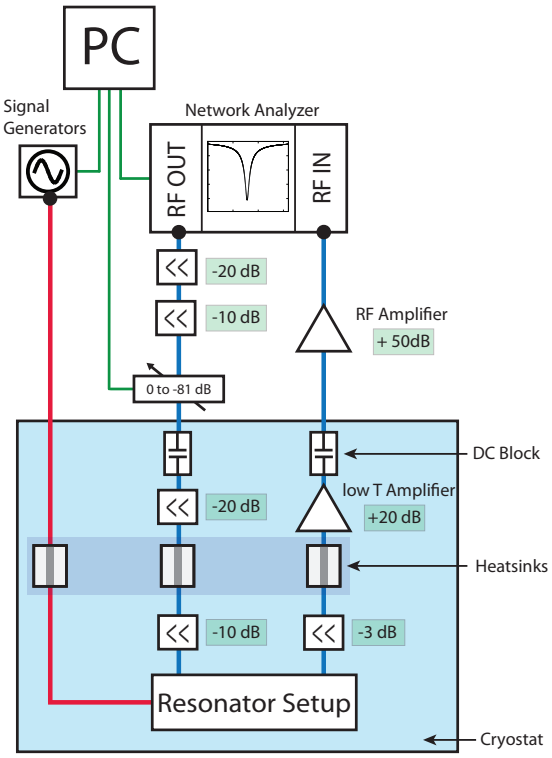

Figure 3.1: Schematic illustration of the radio frequency measurement setup. The components outside of the light blue box are at room temperature while the components inside of it are in the cryostat. The blue path marks the measurement signal line, the red path stands for the application of the bias signal and the green lines indicate the connections to the computer. Adapted from [Stä24].

dered inductance line and is sputter deposited onto the glass sample and provides a resonance frequency of 1.125 GHz. The IDC is made up by 80 1000 μm long and 6 μm wide fingers that are spaced by 2 μm. Their edges are rounded to avoid strong electric field strengths which would lead to non-linearities. The feedline couples the signal of the VNA inductively to the resonator.

The bias electrode sits on top of the resonator and is attached to it in such a way that the bias and the probe field are perpendicular to each other to minimize their coupling. The distance between the bias electrode and the ground plate is $d = 257\,\mu$m. A 127 μm thick Kapton[5] foil ensures that the bias electrode and the resonator are galvanically separated.

The feedline of the resonator and the bias electrode are connected to the coaxial cables through SMA[6] connectors which are bonded to the individual pads on the chip with aluminium wire. Aluminium bonds connect the ground plate of the chip to the sample holder which additionally improves the thermalization of the chip to the mixing chamber.

The glass sample which was used in this thesis is the borosilicate glass BS 3.3[7] and was already used in dielectric measurements in [Vio23]. Its chemical composition can be found in table 3.1.

[5]CMC 70125, DuPont, 974 Centre Rd., Wilmington, DE 19805, USA
[6]Sub-Miniature-A
[7]Th. Geyer GmbH & Co. KG, Dornierstraße 4-6, 71272 Renningen, Germany

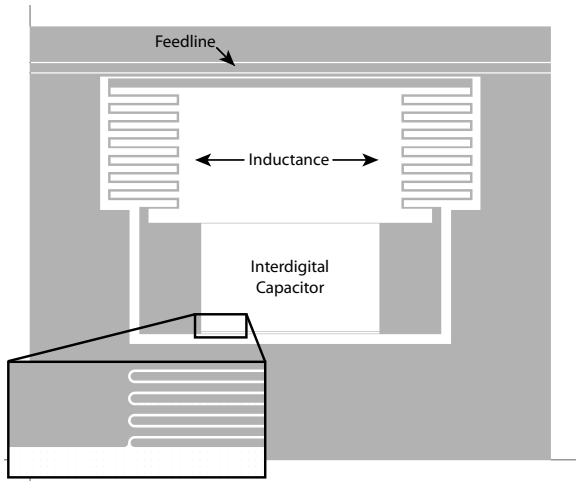

Figure 3.2: Schematic illustration of the circuit of the LC-resonator. The LC-resonator (gray) consists of an interdigital capacitor (IDC) and a meandered inductance line. The VNA is inductively coupled to the resonator through the feedline. Adapted from [Stä24].

SiO_2	B_2O_3	Na_2O	Al_2O_3	K_2O	BaO
83,4%	11,6%	3,4%	1,14%	0.41%	0.005%

Table 3.1: Chemical composition of the borosilicate glass BS 3.3 in molar mass percentage. [Lud03].

3.4 Measurement principle

In this section we explain how the real and imaginary part of the dielectric function can be derived from the resonance frequency and the quality factor of the resonator that probes the glass sample. As the resonator is a LC-circuit its resonance frequency is calculated as

$$f_0 = \frac{1}{2\pi\sqrt{LC}} \tag{3.1}$$

where C is the capacitance and L the inductance. As the resonator does not only probe the sample but also a volume outside of it a parasitric stray capacitance C_p has to be added to capacitance that probes the sample C_x so that we obtain for the total capacitance

$$C = C_\mathrm{x} + C_\mathrm{p} = \varepsilon_\mathrm{r} C_\mathrm{p} + C_\mathrm{p} \quad . \tag{3.2}$$

In the second step of this equation we used the fact that the capacitor is planar so that the capacitance that probes the sample C_x can be written in terms of the relative permittivity ε_r and the parasitric stray capacitance C_p. As the resonance frequency is proportional to the inverse of the square root of the capacitance according to equation 3.1 the relative change of the capacitance can be expressed in terms of the resonance frequency. By choosing C_ref and $f_{0,\mathrm{ref}}$ as arbitrary reference values we

obtain for the relative change of the capacitance

$$\frac{\Delta C}{C} = \frac{C - C_{\mathrm{ref}}}{C_{\mathrm{ref}}} = \left(\frac{f_{0,\mathrm{ref}}}{f_0}\right)^2 - 1 \quad . \tag{3.3}$$

In this thesis, a value of $f_{0,\mathrm{ref}} = 1.126\,\mathrm{MHz}$ was chosen for the arbitrary reference value. A change of the real part of the dielectric function leads to a change of the capacitance of the resonator so that we obtain

$$\frac{\delta\varepsilon'}{\varepsilon'} = \frac{\Delta C_{\mathrm{x}}}{C_{\mathrm{x}}} = \frac{\Delta C}{C}\frac{1}{1 - \frac{C_{\mathrm{p}}}{C}} = \left[\left(\frac{f_{0,\mathrm{ref}}}{f_0}\right)^2 - 1\right]\frac{1}{\mathcal{F}} \tag{3.4}$$

where $\mathcal{F}$ is the filling factor which can be expressed in terms of the relative permittivity ε_{r} using equation 3.2 and reads as

$$\mathcal{F} = 1 - \frac{C_{\mathrm{p}}}{C} = \frac{\varepsilon_{\mathrm{r}}}{\varepsilon_{\mathrm{r}} + 1} \quad . \tag{3.5}$$

The intrinsic quality factor of the resonator Q_{i} is the ratio of the total energy that is stored in the capacitor and the power that is dissipated in one oscillation cycle. Using $P_{\mathrm{dis}} = \frac{U_{\mathrm{ac}}^2}{2R}$ as the dissipated power and $W_0 = \frac{CU_{\mathrm{ac}}^2}{2}$ as the total stored energy we obtain

$$Q_{\mathrm{i}} = 2\pi f_0 \frac{W_0}{P_{\mathrm{dis}}} = R\sqrt{\frac{C}{L}} \tag{3.6}$$

where R is a resistance that results from dissipation processes through atomic tunneling systems and can be handled as parallel to the capacitor. Ohmic and radiation losses can be neglected since the whole resonator is superconducting and coated with niobium. As the resonator also couples to the feedline an additional quality factor Q_{c} has to be introduced so that the inverse of the total quality factor can be calculated as

$$\frac{1}{Q} = \frac{1}{Q_{\mathrm{i}}} + \frac{1}{Q_{\mathrm{c}}} \quad . \tag{3.7}$$

Since the dielectric loss results from dissipation processes in the glass it can be calculated by using the inverse of the intrinsic quality factor. According to equation 3.6 the intrinsic quality factor is proportional to the square root of the capacitance. As the capacitor also probes a volume outside of the glass sample the stray capacitance C_{p} has to be considered when calculating the dielectric loss. Therefore, the dielectric loss reads as

$$\tan\delta = \frac{1}{Q_{\mathrm{i}}}\sqrt{1 + \frac{C_{\mathrm{p}}}{C_{\mathrm{x}}}} = \frac{1}{Q_{\mathrm{i}}\sqrt{\mathcal{F}}} \quad . \tag{3.8}$$

To determine the real and imaginary part of the dielectric function the resonance frequency and the quality factor of the resonator have to be measured. The VNA provides these quantities by measuring the complex valued transmission S_{21}. According to Probst *et al.* [Pro15] the scattering coefficient S_{21} of a notch type resonator is calculated as

$$S_{21}(f) = ae^{\mathrm{i}\alpha}e^{-2\pi\mathrm{i}f\tau}\left(1 - \frac{\frac{Q}{Q_\mathrm{c}}e^{\mathrm{i}\phi}}{1 + 2\mathrm{i}Q\frac{f-f_0}{f_0}}\right) \quad . \tag{3.9}$$

To account for an amplification or attenuation of the signal the scaling parameter a is introduced. α includes phase shifts, τ considers cable delays caused by the finite speed of the signal and the length of the cable and ϕ takes a possible impedance mismatch into account. The line shape of the VNA readout is the absolute value of the complex transmission S_{21} and reads as

$$|S_{21}| = \sqrt{S_{21}S_{21}^*} = a\left(1 - \frac{2\frac{Q}{Q_\mathrm{c}}\left(\cos\phi + 2Q\left(\frac{f-f_0}{f_0}\right)\sin\phi\right) - \left(\frac{Q}{Q_\mathrm{c}}\right)^2}{1 + 4Q^2\left(\frac{f-f_0}{f_0}\right)^2}\right)^{\frac{1}{2}} \quad . \tag{3.10}$$

This function is fitted to the measurement data of the VNA readout to obtain the dielectric response of the glass sample.

3.4.1 Application of a continuous electric bias signal

In this thesis the dielectric response of the used glass sample was measured under the influence of a continuous triangle bias signal. The bias signal is applied by the signal generator which ensures a controllable bias voltage and frequency. In figure 3.3 two exemplary resonance curves of the VNA readout are shown as a function of the frequency of the driving field. By fitting the absolute value of the complex transmission from equation 3.10 to the resonance curves we obtain the resonance frequency and the quality factor from which the real part of the dielectric function and the dielectric loss can be determined. One of the two resonance curves depicted in figure 3.3 was measured without the application of a bias signal whereas the other curve was measured with the application of a bias signal. One can clearly see that the application of a bias signal results in a larger FWHM which corresponds to a lower quality factor and thus a higher dielectric loss according to equation 3.8. From this it can be concluded that the dielectric loss of the probed glass sample can be manipulated by an electric bias field.
The bias rate can be controlled by varying the bias frequency or the bias voltage according to equation 2.69. To obtain a wide range of bias rates the dielectric loss has been measured for 47 bias voltages ranging from 0.1 V to 20 V and for

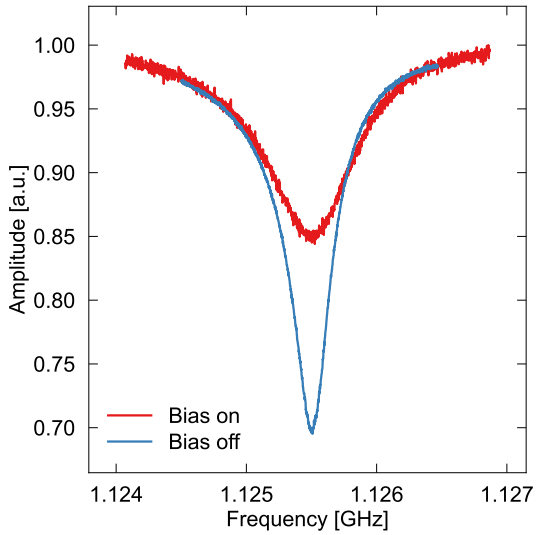

Figure 3.3: Resonance curves of the resonator readout with (red) and without (blue) the application of a bias signal. The increased FWHM of the curve with the bias signal corresponds to a lower quality factor and thus a higher dielectric loss.

bias frequencies spanning from 1 Hz to 7.9 MHz. For increasing bias voltages the maximum bias frequency had to be chosen lower to avoid heating effects which occur at high bias rates. Therefore, the maximum bias frequency for the bias voltage of 20 V could only be 126 kHz. In this sense the bias rates ranged from $\dot{F}_\mathrm{b} \approx 10^{-3}\,\frac{\mathrm{MV}}{\mathrm{m{\cdot}s}}$ to $\dot{F}_\mathrm{b} \approx 10^{4}\,\frac{\mathrm{MV}}{\mathrm{m{\cdot}s}}$.

4. Experimental Results

In this chapter we present the results obtained from the measurements and interpret them within the framework of the standard tunneling model and the Landau-Zener formalism. First we will briefly discuss the power dependence of the dielectric loss. After that we focus on the non-equilibrium measurements where the asymmetry energy of the tunneling systems in the glass sample was manipulated by a continuous bias field. In this section we examine the dielectric loss in terms of different bias parameters. This further allows us to determine the average dipole moment and the average lifetime of the tunneling systems.
All measurements have been carried out at the same temperature of 30 mK. Accordingly, we can assume a good thermalization of the sample to the desired temperature.

4.1 Power dependency

The power dependency measurement of the dielectric loss allows us to determine how the excitation power affects the saturation of tunneling systems and below which power the loss becomes independent of the driving field. In this measurement no bias field has been applied. The power has been varied by a step attenuator so that the dielectric response could be measured for driving powers ranging from $-130\,\mathrm{dBm}$ to $-50\,\mathrm{dBm}$. In figure 4.1 the dielectric loss is shown as a function of the driving field power. The errors of the data points are of statistical nature and result from averaging over a few measurements.
The dependency of the dielectric loss on the driving field power mostly agrees with the expectations of the standard tunneling model. At the lowest powers we observe a plateau in the dielectric loss corresponding to the field independent low power loss from equation 2.44. For increasing powers the dielectric loss decreases because more and more tunneling systems are saturated. The data points can be described by equation 2.41. Due to electric field inhomogeneities and residual losses this fitting function has to be modified. [Kör19] suggested to use the function

$$\tan\delta = A\frac{\tanh\left(\frac{\hbar\omega}{2k_\mathrm{B}T}\right)}{\sqrt{1+\left(\frac{P}{P_\mathrm{c}}\right)^{\beta}}} + C \tag{4.1}$$

to fit the data of the dielectric loss. The parameters are $A = \frac{\pi P_0 p^2}{3\varepsilon_0\varepsilon'}$, P_c, β and C. P_c describes the critical power and C stands for a constant residual dielectric loss

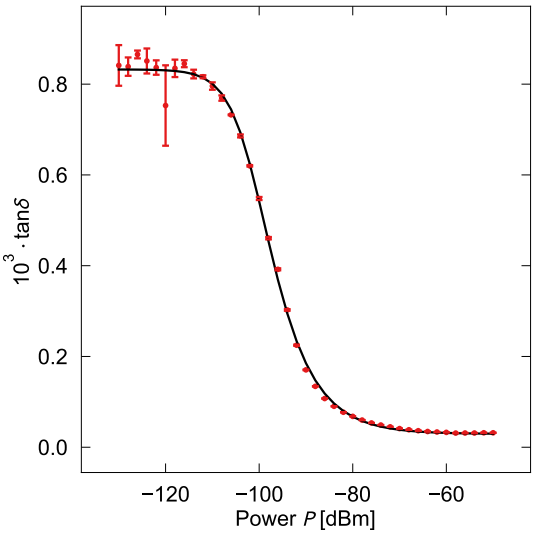

Figure 4.1: Power dependency of the dielectric loss. The data points can be described with the fitting function from equation 4.1 which is depicted as a black line. The dielectric loss is independent of the driving field below a critical driving power of $P_\mathrm{c} = -101.3\,\mathrm{dBm}$.

due to loss contributions which are not considered in the standard tunneling model. Since $P \propto F_\mathrm{ac}^2$ the parameter β should be 1. But due to an inhomogeneity in the electric field of the IDC an increased value for β has been obtained. The values of the parameters determined by the fitting routine are shown in table 4.1.

A	P_c [dBm]	β	C
$(1.121 \pm 0.011) \cdot 10^{-3}$	-101.3 ± 0.3	1.24 ± 0.05	$(2.9 \pm 0.5) \cdot 10^{-5}$

Table 4.1: Parameters obtained by fitting equation 4.1 to the power dependency of the dielectric loss.

4.2 The dielectric loss in terms of the bias rate

The non-equilibrium measurements were conducted for 47 different bias voltages spanning from 0.1 V to 20 V at a constant driving power of $-94\,\mathrm{dBm}$. In figure 4.2 the real part of the dielectric function $\delta\varepsilon'/\varepsilon'$ (left) and the dielectric loss $\tan\delta$ (right) are plotted as a function of the bias rate $\dot{F}_\mathrm{b}$. For the sake of clarity, we start by discussing exemplary curves of the real part and the loss for four different bias voltages. In principle the curves of the dielectric loss follow the behavior predicted by the theory in section 2.4. However, the graph of the dielectric loss for a bias voltage of $U_\mathrm{b} = 20\,\mathrm{V}$ deviates slightly from the theoretical expectation. Before we give an explanation for this we first discuss the behavior of the first three loss curves in the following.

All three curves start approximately at the same saturation limit of $\tan\delta \approx 0.30 \cdot 10^{-3}$.

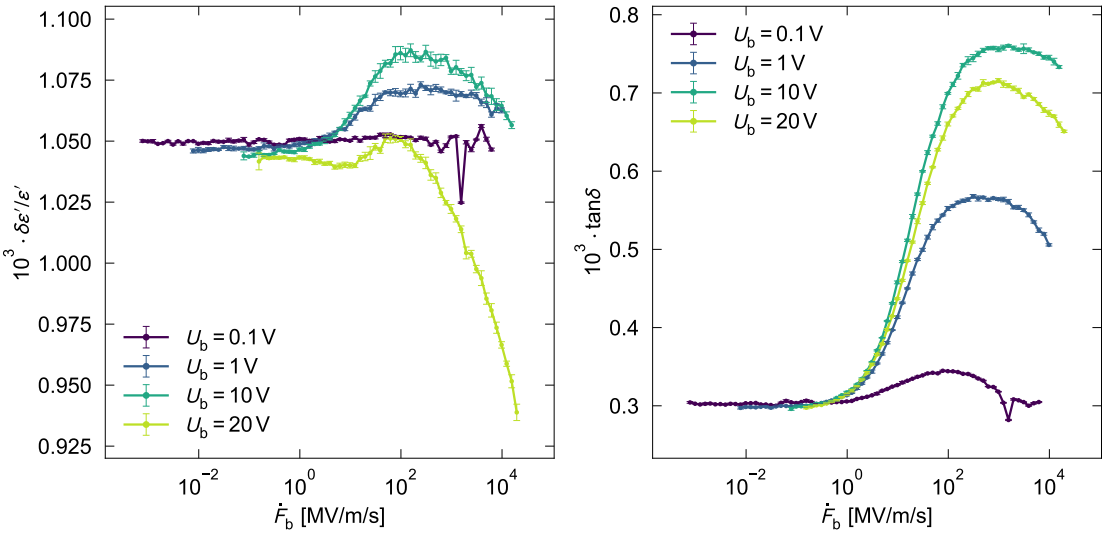

Figure 4.2: Real part of the dielectric function $\delta\varepsilon'/\varepsilon'$ (left) and dielectric loss $\tan\delta$ (right) as a function of the bias rate $\dot{F}_\mathrm{b}$ for four different bias voltages U_b.

In this limit relaxation processes occur during resonant transitions which leads to the constant saturation loss. As the dielectric loss in the quasistatic limit does not deviate from the loss in the non-biased case it can be compared with the power dependency measurement where we find that a dielectric loss of $\tan\delta \approx 0.30 \cdot 10^{-3}$ indeed corresponds to a driving power of $P \approx -94\,\mathrm{dBm}$. The bias field thus has no effect on the dielectric loss in the quasistatic regime. The saturation limit holds up to bias rates of $\dot{F}_\mathrm{b} \approx 1\,\frac{\mathrm{MV}}{\mathrm{m\cdot s}}$.

At higher bias rates all curves experience an increase in the dielectric loss because more tunneling systems perform resonant transitions. This increase is steeper for higher bias voltages. Because the tunneling systems cover a wide range of relaxation times the coherent regime already begins at low bias rates for tunneling systems with the highest relaxation times. As the coherent regime starts at the same bias frequency for all bias voltages it sets in at lower bias rates for lower bias voltages. Therefore, the loss increases less steep for lower bias voltages because transitions of tunneling systems with high relaxation times result in a weakening of the increase of the dielectric loss.

For further increasing bias rates the increase of the dielectric loss slows down and eventually reaches a maximum. The value of the maximum increases with increasing bias voltages which can again be explained by transitions of tunneling systems with high relaxation times which result in a lower maximum at lower bias voltages. Whereas the dielectric loss at the lowest bias voltage starts to decrease after reaching the maximum we observe more of a plateau in the dielectric loss for the higher bias voltages. Also the maximum loss is reached at higher bias rates for higher bias

voltages. As the single ramp limit holds up to higher bias rates for higher bias field strengths the occurrence of the plateaus can be explained within the single ramp limit. At high bias rates more tunneling systems are swept through the resonance while more of them perform Landau-Zener transitions resulting in the dielectric loss reaching a plateau. As can be seen in in figure 4.2 the maximum loss is reached at a bias voltage of $U_\mathrm{b} = 10\,\mathrm{V}$. By comparing the maximum of the loss curve for $U_\mathrm{b} = 10\,\mathrm{V}$ which is $\tan\delta = 0.76 \cdot 10^{-3}$ with the field independent low power limit from the power dependency measurement which is $\tan\delta_0 \approx 0.83 \cdot 10^{-3}$ we find that the maximum dielectric loss is slightly smaller than the low power limit. The reason for the dielectric loss being lower in the biased case can be addressed to heating effects caused by the high bias rate. This can be confirmed by figure 2.7 where an increasing temperature results in a decreasing resonant contribution to the dielectric loss.
After reaching the maximum the loss curve at the lowest bias voltage drops back to the saturation limit. To explain the decrease of the dielectric loss at the lower bias voltages we must switch from the single ramp limit to the coherent limit where successive transitions interfere with each other because the bias period is shorter than the relaxation time $T_\mathrm{b} \ll \tau_1$. For increasing bias frequencies more and more transitions interfere destructively with each other so that the dielectric loss decreases and eventually reaches the same value as the saturation limit. Because of the small bias voltage of $U_\mathrm{b} = 0.1\,\mathrm{V}$ this coherent limit sets in at lower bias rates.
The dielectric loss at the lowest bias voltage experiences a dip at a high bias rate. As we will see later this dip can be seen in all curves at lowest bias voltages. As these dips occur at the same bias frequency they may be caused by a frequency selective heating effect.

Until now only the behavior of the dielectric loss for the first three bias voltages has been explained. In this sense we will continue to explain the deviating behavior of the dielectric loss for the highest bias voltage of $U_\mathrm{b} = 20\,\mathrm{V}$. At first glance the dielectric loss seems to follow the theoretical expectations. This is true for low bias rates as the curve of the dielectric loss for the highest bias voltage also starts at the same saturation limit as the other three curves. However, as the bias rate increases the dielectric loss for $U_\mathrm{b} = 20\,\mathrm{V}$ experiences a less steep increase and a lower maximum than the loss curve for $U_\mathrm{b} = 10\,\mathrm{V}$ even though the bias voltage is higher. This deviation is probably caused by heating effects due to the high bias field strength.

The real part of the dielectric function can be used to verify the heating effects discussed in the last few paragraphs. As can be seen in figure 2.5, mainly off resonant tunneling systems contribute to the real part of the dielectric function. Consequently, the real part should be nearly constant for all bias rates. As can be seen

in figure 4.2, this is not the case. Only at low bias rates all curves are constant. This is not surprising since most likely no heating effects occur at low bias rates. At higher bias rates the real part starts to increase at the same bias rate as the loss and slightly follows the course of the loss curves. The reason for that may be a net excess saturation of low energetic tunneling systems due to biasing [Bli24]. The real part decreases again at the highest bias rates. Especially the curve for the highest bias voltage decreases very steeply which confirms the assumed heating effect. In contrast, the curve at the lowest bias voltage is fairly constant within the whole bias rate range. This confirms that the decrease of the dielectric loss at high bias rates can be explained within the coherent regime and is not caused by a heating of the sample. The only exception is one dip at a high bias rate. This dip of the real part corresponds to the dip of the dielectric loss discussed earlier which confirms the assumed frequency selective heating effect.

4.2.1 Two dimensional map of the dielectric loss

The discussion in the previous section only covered the real part of the dielectric function and the dielectric loss for four different bias voltages within the range from 0.1 V to 20 V. However, the dielectric response of the the sample has been measured for 47 different bias voltages in this range. As it would be rather confusing to show 47 curves in one diagram we follow another approach to show all measured curves in a clearly presented way. By choosing the bias voltage to be on the y-axis and the bias rate to be on the x-axis we can make a two-dimensional map where every (x,y)-coordinate corresponds to a bias rate-, bias voltage-pair. The color of the data points correspond to the real part of the dielectric function and the dielectric loss. The map of the loss is shown in figure 4.3 and the map of the real part in figure 4.4.

The observations of the previous section can also be taken here. As can be seen in figure 4.3, the dielectric loss approaches the same saturation limit at low bias rates for all bias voltages and starts to increase at approximately the same bias rate of $\dot{F}_\mathrm{b} \approx 1 \frac{\mathrm{MV}}{\mathrm{m \cdot s}}$. The maximum of the dielectric loss is reached at a bias voltage around $U_\mathrm{b} \approx 10\,\mathrm{V}$. For higher bias voltages the maximum starts to decrease which is probably caused by a heating effect. The bias rate at which the maximum occurs is at $\dot{F}_\mathrm{b} \approx 10^2 \frac{\mathrm{MV}}{\mathrm{m \cdot s}}$ for low bias voltages and increases with increasing bias voltages so that the maximum for bias voltages at around $U_\mathrm{b} \approx 10\,\mathrm{V}$ can be found at bias rates around $\dot{F}_\mathrm{b} \approx 10^3 \frac{\mathrm{MV}}{\mathrm{m \cdot s}}$. The reason for this is that for the lowest bias voltages the dielectric loss drops back to the saturation limit at highest bias rates because there the coherent limit is reached earlier where successive transitions interfere with each other. For higher bias voltages the coherent limit is reached at higher bias rates so that the dielectric loss decreases again at higher bias rates. However, the single

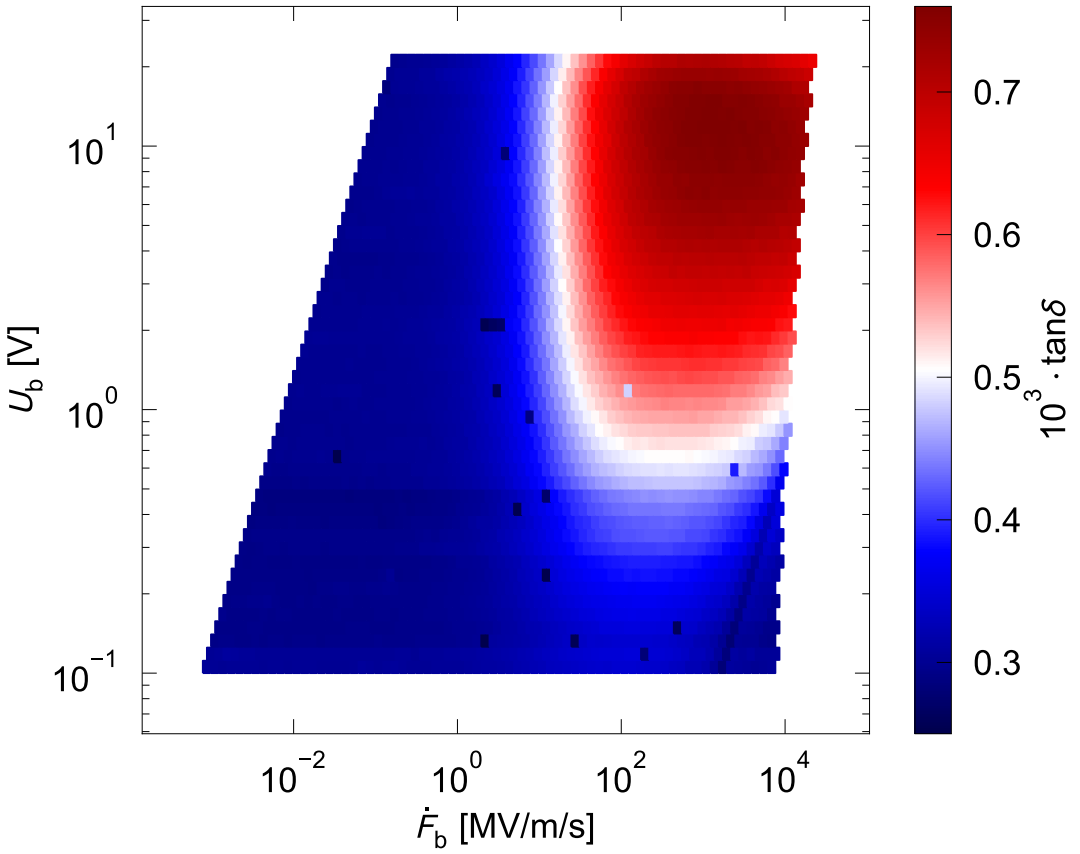

Figure 4.3: Map of the dielectric loss. The y-axis corresponds to the bias voltage and the x-axis to the bias rate. The dielectric loss can be determined by the color of the dots.

ramp limit where a plateau should occur at highest bias rates might be still applicable there so that the coherent limit is not reached for the highest bias voltages. Therefore, the decrease of the dielectric loss at highest bias rates can most likely be addressed to a heating of the sample.

As can be seen in figure 4.4, the real part of the dielectric function is the lowest at highest bias voltages and bias rates. This supports the previous made assumption that heating effects cause the dielectric loss to decrease at highest bias voltages and bias rates. For lower bias rates and bias voltages the real part should be constant as no heating effects are assumed to be there. However, this is not the case as the real part increases for bias voltages above $U_\mathrm{b} \approx 0.5\,\mathrm{V}$ and bias rates above $\dot{F}_\mathrm{b} \approx 1\frac{\mathrm{MV}}{\mathrm{m \cdot s}}$. This increase occurs at the same bias rate as the increase of the dielectric loss. As already mentioned, the reason for this may be a net excess saturation of low energetic tunneling systems due to biasing [Bli24]. Only for bias voltages below $U_\mathrm{b} \approx 0.5\,\mathrm{V}$ the real part of the dielectric function is approximately constant over the whole range

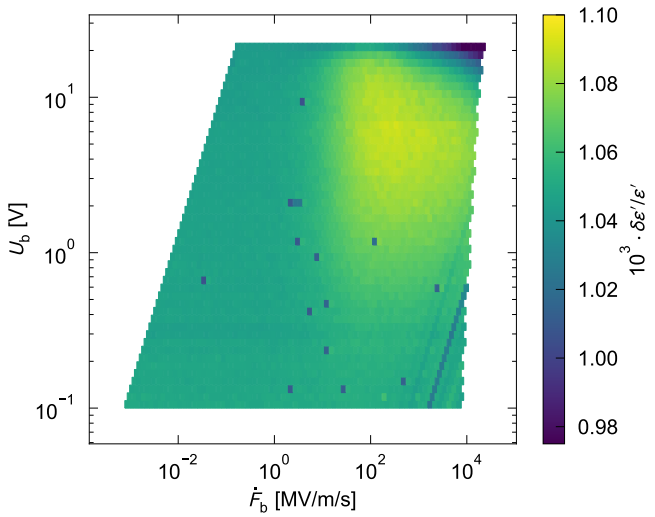

Figure 4.4: Map of the real part of the dielectric function. The y-axis corresponds to the bias voltage and the x-axis to the bias rate. The real part can be determined by the color of the dots.

of bias rates with the exception of one line in the map that is much lower than the real part around it. This sudden dip also occurs in the dielectric loss and is always observed at the same bias frequency of $f_b \approx 2\,\mathrm{MHz}$ for both the real part and the loss. Another line at which the real part of the dielectric function is lower than the real part around it can be seen at a bias frequency of $f_b \approx 800\,\mathrm{kHz}$. This sudden dip cannot be observed in the dielectric loss which may result from the fact that this line is barely recognizable in the real part. As these dips each occur at the same bias frequency they might be addressed to frequency selective heating effects. Possible reasons for this may be resonances near the experimental setup.

A few randomly distributed outliers can be seen in the map of the real part of the dielectric function and in the map of the dielectric loss. These outliers are at the same bias voltages and bias rates in both maps. The reason for the occurrence of these outliers can be addressed to an incorrect execution of the measurement. The resonance curves have not been measured for the whole range of the driving field frequency so that the function from equation 3.10 could not be fitted appropriately to the measurement data obtained at these bias voltages and bias rates.

4.3 The dielectric loss in terms of the dimensionless bias rate

When we plot the dielectric loss in terms of the dimensionless bias rate ξ (equation 2.66) we can compare the loss curve with the theory curve from equation 2.67. For this comparison it is useful to choose a loss curve with a high bias field strength, i.e. a high bias voltage, because there the single ramp limit holds up to high bias rates allowing the dielectric loss to reach the fully desaturated limit where the effects of

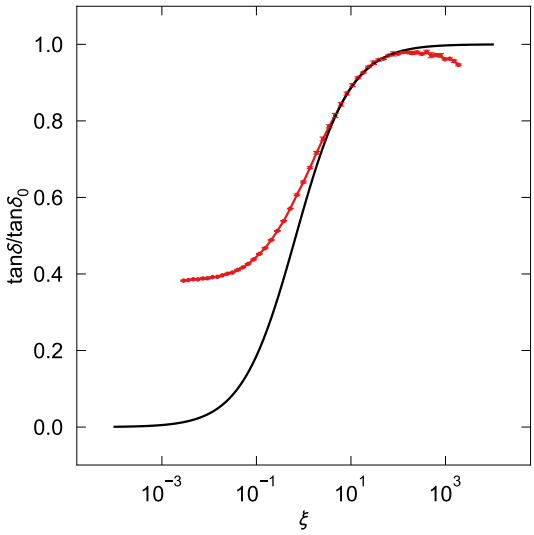

Figure 4.5: Plot of the normalized dielectric loss $\tan\delta/\tan\delta_0$ (red) for a bias voltage of $U_\mathrm{b} = 11.22\,\mathrm{V}$ and the theoretical loss curve (black) (equation 2.67) for an average dipole moment of $p = 0.31\,\mathrm{D}$ as a function of the dimensionless bias rate.

more tunneling systems being swept through the transition region and more Landau-Zener transitions cancel each other out. However, choosing the loss curve with the highest bias voltage is not suitable because there the dielectric loss decreases at high bias rates due to possible heating effects. Therefore, the measurement of the dielectric loss at a bias voltage of $U_\mathrm{b} = 11.22\,\mathrm{V}$ is chosen because for this bias voltage the dielectric loss has the highest maximum of all calculated loss curves. The dimensionless bias rate has one freely adjustable parameter which is the average dipole moment p. Adjusting this parameter in a way that the shape of the loss curve from the measurement data agrees with the shape of the theoretical loss curve allows us to determine the average dipole moment of the tunneling systems in the glass sample. A plot of the normalized dielectric loss $\tan\delta/\tan\delta_0$ for a bias voltage of $U_\mathrm{b} = 11.22\,\mathrm{V}$ and the theoretical loss curve can be seen in figure 4.5. In this plot an average dipole moment of

$$p = 0.31\,\mathrm{D} \tag{4.2}$$

has been found to be the best fit for the data.

Another use of plotting the dielectric loss in terms of the dimensionless bias rate is to compare time and energy scales of the tunneling systems and the bias field. For this the three critical bias rates have to be estimated in order to obtain the average lifetime of the tunneling systems in the used glass sample. The most intuitive way is to start with the second critical bias rate ξ_2 (equation 2.71) which marks the transition from the single ramp limit to the continuous regime where the bias period becomes smaller than the relaxation time so that successive transitions interfere with each other. For low bias field strengths ξ_2 is just before reaching the maximum loss because for higher bias rates more and more transitions interfere destructively

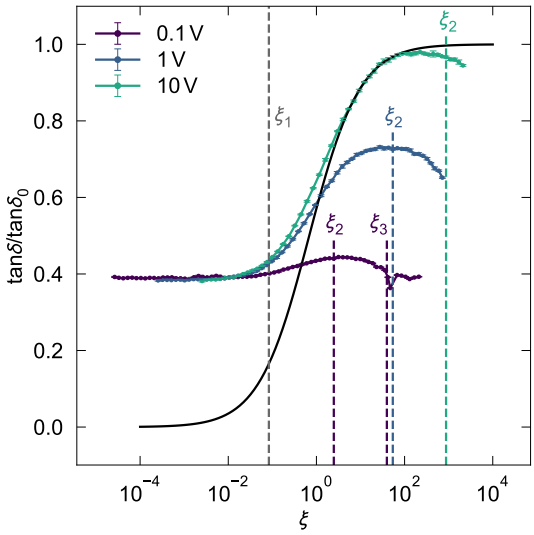

Figure 4.6: Normalized dielectric loss for three different bias voltages as a function of the dimensionless bias rate. The theoretical loss curve is depicted as a black line for comparison. The first critical bias rate is marked as a dashed gray line and labeled with ξ_1. The second and third critical bias rates are marked as dashed lines and labeled with ξ_2 and ξ_3 respectively and are colored with the same color as the loss curves which they correspond to.

with each other resulting in the loss reaching the maximum and decreasing again. Therefore, the loss curve at the lowest bias voltage of $U_\mathrm{b} = 0.1\,\mathrm{V}$ has been chosen to estimate the second critical bias rate at this bias voltage. As ξ_2 is proportional to the bias field strength according to equation 2.71 it is different for every bias voltage. Hence, to calculate ξ_2 for every bias voltage by using equation 2.71 the average lifetime of the tunneling systems has to be determined from our estimated ξ_2. As ξ_2 marks the bias rate at which it equals the inverse lifetime of a tunneling system τ_1^{-1} the average lifetime of the tunneling systems τ can be calculated by the inverse of the bias frequency f_b that corresponds to ξ_2. Through this method an average lifetime of the tunneling systems of

$$\tau \approx 13\,\mu\mathrm{s} \tag{4.3}$$

could be determined. In figure 4.6 the second critical bias rates for the three depicted loss curves are marked as dashed lines whose color match the color of the corresponding loss curve. For increasing bias voltages ξ_2 is higher. One would expect that a plateau should form at highest bias rates for $U_\mathrm{b} = 10\,\mathrm{V}$ because the fully desaturated limit of the single ramp regime is reached before the coherent regime sets in which causes a decrease of the dielectric loss. However, this is not the case since the dielectric loss starts to decrease before the second critical bias rate is reached. A reason for that may be slight heating effects caused by the high bias field strength and bias frequency resulting in the decrease of the dielectric loss.
According to equation 2.68 the first critical bias rate does not depend on the bias field strength so that it is equal for every bias voltage. To calculate ξ_1 using equation 2.68 the driving field strength at the lowest bias rate is chosen because there the saturation limit is valid where relaxation processes occur during resonant transitions. By using the average lifetime of the tunneling systems determined above the first

critical bias rate is calculated as $\xi_1 \approx 0.083$ and marked as a gray dashed line in figure 4.6. One can see that ξ_1 marks the point where the dielectric loss starts to increase. Below ξ_1 relaxation processes occur during resonant transitions resulting in the dielectric loss reaching a plateau. Above ξ_1 the single ramp limit is valid where the increasing bias rates result in an increasing dielectric loss.
The third critical bias rate ξ_3 corresponds to the bias rate at which the dielectric loss returns back to the same constant value as it was reached in the saturation limit. However, this happens only for the lowest bias voltages. Therefore, the driving field strength at the lowest bias rate is chosen for the calculation of ξ_3 using equation 2.72 because at the lowest bias rates all loss curves start at the same saturation limit. In figure 4.6 the third critical bias rate is shown for the loss curve at the lowest bias voltage and is marked as a dashed line whose color matches the color of the corresponding loss curve. The third critical bias rates for the other bias voltages are not inside the measured bias rate range and are thus not shown in figure 4.6. If the dielectric loss would have been measured up to higher bias rates a decrease of it could not only be addressed to the reaching of the same value as the saturation limit but also possible heating effects could lead to a decrease of the loss.

5. Summary and Outlook

In this thesis the influence of a periodic electric bias field on the dielectric loss of atomic tunneling systems in the borosilicate glass BS 3.3 was investigated. For that the tunneling systems in the sample were probed at a resonance frequency of 1.125 GHz using a resonator which was sputter deposited onto the glass sample. The experiment was placed in a cryostat to ensure a temperature of 30 mK and the resonator was read out by a VNA to determine the dielectric function from which the dielectric loss can be obtained. To induce non-equilibrium Landau-Zener dynamics of the tunneling systems a bias field is applied through a cover electrode that sits on top of the sample.

First, the driving power dependency of the dielectric loss was measured which agreed well with the predictions of the standard tunneling model. At low powers the expected plateau as well as the decrease for increasing powers could be observed. Accordingly, a modified function of the saturation loss, which additionally accounts for electric field inhomogeneities and residual losses could be fitted quite well to the data points.
The main part of this thesis were non-equilibrium measurements in which the asymmetry energy of the tunneling systems was manipulated by the bias field. The parameters of the bias field which were varied in order to determine their influence on the dielectric loss were the bias voltage and the bias frequency. In principle, the dielectric loss followed the behavior predicted by the Landau-Zener theory. At low bias rates the loss approached the saturation limit and increased for increasing bias rates for all bias voltages. After reaching a maximum, the dielectric loss dropped back to the saturation limit at high bias rates for the lowest bias voltages which could be explained within the framework of the interference of coherent resonant transitions. For higher bias voltages, the dielectric loss reached more of a plateau at high bias rates which corresponds to the fully desaturated limit in the single ramp regime. The decrease of the loss at the highest bias rates and bias voltages could be explained by a possible heating of the sample. The centerpiece of this thesis was the two-dimensional map of the dielectric loss in which the loss was plotted in terms of the bias voltage and the bias rate. This map verified the observations and conclusions which have already been taken from the loss curves that were plotted at different bias voltages.
In a last step, the dielectric loss was plotted in terms of the dimensionless bias rate which allowed us to compare the obtained dielectric loss curve with the curve from the Landau-Zener theory to extract microscopic quantities of tunneling systems.

Thereby, an average dipole moment of $p = 0.31\,\mathrm{D}$ could be determined. Furthermore different critical bias rates were estimated to compare the time and energy scales of the saturation limit, the single ramp regime and the coherent regime. In this context, an average lifetime of the tunneling systems of $\tau \approx 13\,\mu\mathrm{s}$ could be estimated.

The obtained results agree with measurements conducted on the same glass by Viol [Vio23] and measurements and simulations conducted on the glass N-BK7 by Blickberndt [Bli22]. In further experiments the dielectric loss could be measured up to higher bias rates to obtain the expected return to the saturation limit also for high bias voltages. However, it is crucial to eliminate the heating effects at high bias rates and bias voltages for these measurements to obtain useful measurement results. Another possible experiment could be exposing the glass BS 3.3 to mechanical strain fields which also change the asymmetry energy of tunneling systems. This would allow for a deeper understanding of non equilibrium Landau-Zener dynamics induced by acoustic biasing.

Bibliography

[And72] P. W. Anderson, B. I. Halperin, and C. M. Varma, Anomalous Low-temperature Thermal Properties of Glasses and Spin Glasses, *Phil. Mag.*, **25**, 1, 1972.

[Bli22] J. Blickberndt, *The Influence of Continuous Electric Bias Fields on the Dielectric Loss of Atomic Tunneling Systems*, Master thesis, Heidelberg University, 2022.

[Bli24] J. Blickberndt, Private Communication, 2024.

[Bur13] A. L. Burin, M. S. Khalil, and K. D. Osborn, Universal Dielectric Loss in Glass from Simultaneous Bias and Microwave Fields, *Phys. Rev. Lett.*, **110**, 157002, 2013.

[Bur14] Alexander L Burin, Andrii O Maksymov, and Kevin D Osborn, Quantum coherent manipulation of two-level systems in superconducting circuits, *Supercond. Sci. Tech.*, **27**(8), 084001, 2014.

[Car94] H. M. Carruzzo, E. R. Grannan, and C. C. Yu, Nonequilibrium dielectric behavior in glasses at low temperatures: Evidence for interacting defects, *Phys. Rev. B*, **50**, 6685–6695, 1994.

[Cla94] J. Classen, C. Enss, C. Bechinger, G. Weiss, and S. Hunklinger, Low frequency acoustic and dielectric measurements on glasses, *Ann. Physik*, **3**, 315, 1994.

[Cla00] J. Classen, T. Burkert, C. Enss, and S. Hunklinger, Anomalous Frequency Dependence of the Internal Friction of Vitreous Silica, *Phys. Rev. Lett.*, **84**, 2176–2179, 2000.

[Deb12] P. Debye, Zur Theorie der spezifischen Wärmen, *Ann. Physik*, **344**, 789, 1912.

[Deb13] P. Debye, On the theory of anomalous dispersion in the region of long-wave electromagnetic radiation, *Verh. Deut. Phys. Gesell.*, **15**, 777–793, 1913.

[Ens05] C. Enss and S. Hunklinger, *Low-Temperature Physics*, Springer, Heidelberg, 2005.

[Fre21] B. Frey, *Landau-Zener spectroscopy of bulk glasses*, Dissertation, Heidelberg University, 2021.

[Fro77] G. Frossati, J. le G. Gilchrist, J. C. Lasjaunias, and W. Meyer, Spectrum of low-energy dipolar states in hydrated vitreous silica, *J. Phys. C*, **10**(18), L515–L519, 1977.

[Fro92] G. Frossati, Experimental techniques: Methods for cooling below 300 mK, *J. Low Temp. Phys.*, **87**(3-4), 595–633, 1992.

[Hun72] S. Hunklinger, W. Arnold, St. Stein, R. Nava, and K. Dransfeld, Saturation of the ultrasonic absorption in vitreous silica at low temperatures, *Phys. Lett. A*, **42**(3), 253 – 255, 1972.

[Hun74] S. Hunklinger, Ultrasonics in Amorphous Materials, *Proc. Ultrasonic Symp. (IEEE)*, 1974.

[Hun76] S. Hunklinger and W. Arnold, 3 - Ultrasonic properties of glasses at low temperatures, Volumen 12 in *Phys. Acoust.*, 155 – 215, Academic Press, 1976.

[Hun77] S. Hunklinger, Acoustic and dielectric properties of glasses at low temperatures, in J. Treusch (Ed.), *Festkörperprobleme 17*, Volumen 17 in *Adv. Solid State Phys.*, 1–11, Springer Berlin Heidelberg, 1977.

[Hun23] Siegfried Hunklinger and Christian Enss, *Festkörperphysik*, De Gruyter Studium, De Gruyter Oldenbourg, München ; Wien, 6th edition, 2023.

[Iva22] O. V. Ivakhnenko, S. N. Shevchenko, and F. Nori, Quantum Control via Landau-Zener-Stückelberg-Majorana Transitions, 2022.

[Jä72] J. Jäckle, On the ultrasonic attenuation in glasses at low temperatures, *Z. Phys. A*, **257**(3), 212, 1972.

[Kha13] M. S. Khalil, *A study of two-level system defects in dielectric films using superconducting resonantors*, Dissertation, University of Maryland, 2013.

[Kör19] D. Körner, *Nichtgleichgewichtsdynamik von Tunnelsystemen im Bor-Kronglas N-BK7 bei* 1 GHz *und tiefen Temperaturen*, Bachelor thesis, Heidelberg University, 2019.

[Ku05] Li-Chung Ku and C. C. Yu, Decoherence of a Josephson qubit due to coupling to two-level systems, *Phys. Rev. B*, **72**, 024526, 2005.

[Lan32] LD Landau, On the theory of transfer of energy at collisions ii, *Phys. Z. Sowjetunion*, **2**(46), 118, 1932.

[Lis15] J. Lisenfeld, G. J. Grabovskij, C. Müller, J. H. Cole, G. Weiss, and A. V. Ustinov, Observation of directly interacting coherent two-level systems in an amorphous material, *Nat. Commun.*, **6**, 2015.

[Luc16] A. Luck, *Nuclear spin dominated relaxation of atomic tunneling systems in glasses*, Dissertation, Heidelberg University, 2016.

[Lud03] S. Ludwig, P. Nagel, S. Hunklinger, and C. Enss, Magnetic Field Dependent Coherent Polarization Echoes in Glasses, *J. Low Temp. Phys.*, **131**, 89–111, 2003.

[Maj32] E. Majorana, Atomi orientati in campo magnetico variabile, *Il Nuovo Cimento*, **9**(43), 1932.

[Mat19] S. Matityahu, H. Schmidt, A. Bilmes, A. Shnirman, G. Weiss, A. V. Ustinov, M. Schechter, and J. Lisenfeld, Dynamical decoupling of quantum two-level systems by coherent multiple Landau–Zener transitions, *npj Quantum Inf.*, **5**, 114, 2019.

[Mü19] C. Müller, J. H. Cole, and J. Lisenfeld, Towards understanding two-level-systems in amorphous solids: insights from quantum circuits, *Rep. Prog. Phys.*, **82**(12), 124501, 2019.

[Nei13] C. Neill, A. Megrant, R. Barends, Yu Chen, B. Chiaro, J. Kelly, J. Y. Mutus, P. J. J. O'Malley, D. Sank, J. Wenner, T. C. White, Yi Yin, A. N. Cleland, and J. M. Martinis, Fluctuations from edge defects in superconducting resonators, *Appl. Phys. Lett.*, **103**(7), 072601, 2013.

[Phi72] W. A. Phillips, Tunneling States in Amorphous Solids, *J. Low Temp. Phys.*, **7**, 351–360, 1972.

[Phi81] W. A. Phillips (Ed.), *Amorphous solids*, Volumen 24 in *Topics in current physics*, Springer, Heidelberg, 1981.

[Pob07] F. Pobell, *Matter and methods at low temperatures*, Springer, Berlin ; Heidelberg, 3. edition, 2007.

[Pro15] S. Probst, F. B. Song, P. A. Bushev, A. V. Ustinov, and M. Weides, Efficient and robust analysis of complex scattering data under noise in microwave resonators, *Rev. Sci. Instrum.*, **86**(2), 024706, 2015.

[Rog97] S. Rogge, D. Natelson, B. Tigner, and D. D. Osheroff, Nonlinear dielectric response of glasses at low temperature, *Phys. Rev. B*, **55**(17), 11256, 1997.

[Sar16] B. Sarabi, A. N. Ramanayaka, A. L. Burin, F. C. Wellstood, and K. D. Osborn, Projected Dipole Moments of Individual Two-Level Defects Extracted Using Circuit Quantum Electrodynamics, *Phys. Rev. Lett.*, **116**, 167002, 2016.

[Sei18] A. Seiler, *Einfluss der Leitungselektronen auf die Dynamik atomarer Tunnelsysteme in ungeordneten Festkörpern*, Dissertation, Karlsruher Institut für Technologie, 2018.

[Stä24] C. Ständer, Private Communication, 2024.

[Stü32] J. Stückelberg, Theorie der unelastischen Stösse zwischen Atomen, *Helv. Phys. Acta*, **5**, 369, 1932.

[Vio23] J. Viol, *Dielectric Measurements on the Borosilicate Glass BS 3.3 in the GHz-Range at Low Temperatures*, Bachelor thesis, Heidelberg University, 2023.

[vS77] M. von Schickfus and S. Hunklinger, Saturation of the dielectric absorption of vitreous silica at low temperatures, *Phys. Lett.*, **64 A**(1), 144, 1977.

[Zac32] W. H. Zachariasen, The Atomic Arrangement In Glass, *J. Am. Chem. Soc.*, **54**(10), 3841–3851, 1932.

[Zel71] R. C. Zeller and R. O. Pohl, Thermal Conductivity and Specific Heat of Noncrystalline Solids, *Phys. Rev. B*, **4**(6), 2029, 1971.

[Zen32] Clarence Zener and Ralph Howard Fowler, Non-adiabatic crossing of energy levels, *Proc. R. Soc. London*, **137**(833), 696–702, 1932.

Acknowledgments

Diese Arbeit wäre ohne die Unterstützung vieler Menschen nicht möglich gewesen. Mein besonderer Dank gilt:

Prof. Dr. Christian Enss für die Möglichkeit, in seine Arbeitsgruppe zu kommen und an solch spannender Forschung teilzuhaben,

PD Dr. Loredana Gastaldo für die unkomplizierte Übernahme der Zweitkorrektur dieser Arbeit,

Dr. Andreas Reiser für die begeisternde Einführung in die Kernquadrupolresonanzspektroskopie und das Korrekturlesen meiner Arbeit,

Christian Ständer für die ausführliche Einführung in das Labor und das Experiment und die Hilfsbereitschaft bei allen möglichen Fragen,

Jan Blickberndt für die unglaubliche Hilfe bei der Auswertung meiner Messergegnisse, das verständliche Erklären selbst komplizierter Sachverhalte und das detaillierte Korrekturlesen meiner Arbeit,

dem Büro 0.311, bestehend aus Christian Ständer, Marta Kruhlik, Jan Blickberndt, Nathalie Probst und Anton Jarecka für die angenehme Atmosphäre und die vielen netten und spannenden Gespräche über physikalische und nichtphysikalische Themen,

Rudi Eitel für die zuverlässige Bereitstellung von flüssigem Helium, ohne das die Experimente niemals möglich wären,

allen Mitgliedern der Arbeitsgruppen F3 und F4 für die nette Zeit, sei es bei Gesprächen während der täglichen Mittagspause oder Unternehmungen wie der Frühjahrstagung,

meiner Familie für die grenzenlose Unterstützung während meines Studiums und darüber hinaus und meinen Freunden, die meine Zeit in Heidelberg auf unglaubliche Weise bereichert haben.

Ich versichere, dass ich diese Arbeit selbstständig verfasst und keine anderen als die angegebenen Quellen und Hilfsmittel benutzt habe.

Heidelberg, den 30.05.2024 .....

(Valentin Hell)